

Evidence for free oxygen in the Neoproterozoic ocean based on coupled iron–molybdenum isotope fractionation

Andrew D. Czaja^{a,b,*}, Clark M. Johnson^{a,b}, Eric E. Roden^{a,b}, Brian L. Beard^{a,b},
Andrea R. Voegelin^c, Thomas F. Nägler^c, Nicolas J. Beukes^d, Martin Wille^e

^a Department of Geoscience, 1215 W. Dayton Street, University of Wisconsin, Madison, WI 53706, USA

^b NASA Astrobiology Institute, University of Wisconsin, Madison, WI 53706, USA

^c Institut für Geologie, Universität Bern, Baltzerstrasse 3, CH-3012 Bern, Switzerland

^d Paleoproterozoic Mineralization Research Group, Department of Geology, University of Johannesburg,
P.O. Box 524, Auckland Park, South Africa

^e Department of Geosciences, Universität Tübingen, Wilhelmstraße 56, 72076 Tübingen, Germany

Received 16 December 2011; accepted in revised form 1 March 2012; available online 14 March 2012

Abstract

Most geochemical proxies and models of atmospheric evolution suggest that the amount of free O₂ in Earth's atmosphere stayed below 10⁻⁵ present atmospheric level (PAL) until the Great Oxidation Event (GOE) that occurred between ~2.2 and 2.4 Ga, at which time free O₂ in the atmosphere increased to approximately 10⁻¹ to 10⁻² PAL. Although photosynthetically produced "O₂ oases" have been proposed for the photic zone of the oceans prior to the GOE, it has been difficult to constrain absolute O₂ concentrations and fluxes in such paleoenvironments. Here we constrain free O₂ levels in the photic zone of a Late Archean marine basin by the combined use of Fe and Mo isotope systematics of Ca–Mg carbonates and shales from the 2.68 to 2.50 Ga Campbellrand–Malmani carbonate platform of the Kaapvaal Craton in South Africa. Correlated Fe and Mo isotope compositions require a key role for Fe oxide precipitation via oxidation of aqueous Fe(II) by photosynthetically-derived O₂, followed by sorption of aqueous Mo to the newly formed Fe oxides. A dispersion/reaction model illustrates the effects of Fe oxide production and Mo sorption to Fe oxides, and suggests that a few to a few tens of μM free O₂ was available in the photic zone of the Late Archean marine basin, consistent with some previous estimates. The coupling of Fe and Mo isotope systematics provides a unique view into the processes that occurred in the ancient shallow ocean after production of free O₂ began, but prior to oxygenation of the deep ocean, or significant accumulation of free O₂ in the atmosphere. These results require oxygenic photosynthesis to have evolved by at least 2.7 Ga and suggest that the Neoproterozoic ocean may have had a different oxygenation history than that of the atmosphere. The data also suggest that the extensive iron formation deposition that occurred during this time was unlikely to have been produced by anoxygenic photosynthetic Fe(II) oxidation. Finally, these data indicate that the ocean had significant amounts of O₂ at least 150 Myr prior to previously proposed "whiffs" of O₂ at the Archean to Proterozoic transition.

© 2012 Elsevier Ltd. All rights reserved.

1. INTRODUCTION

Development of free O₂ in Earth's oceans and atmosphere reflects a major milestone in the evolution of life.

* Corresponding author at: Department of Geoscience, 1215 W. Dayton Street, University of Wisconsin, Madison, WI 53706, USA. Tel.: +1 608 262 4255; fax: +1 608 262 0693.

E-mail address: aczaja@geology.wisc.edu (A.D. Czaja).

Although some geologic evidence indicates significant free O₂ may have existed in Earth's atmosphere and oceans much earlier than 2.4 Ga, perhaps as far back as ~3.8 Ga (e.g., Towe, 1994; Ohmoto, 1996; Ohmoto et al., 2006; Hoashi et al., 2009), the majority of models for Earth's atmospheric evolution, and evidence from the geologic record, indicate that the atmosphere was virtually devoid of free O₂ in the Archean. The first major increase in

atmospheric O₂ content, between ~2.45 and 2.2 Ga, has been termed the “Great Oxidation Event” (GOE) (e.g., Holland, 1984, 2006; Canfield, 2005; Kump and Barley, 2007), the timing of which is constrained, in large part, by mass-independent fractionations of sulfur isotopes (Farquhar et al., 2000), which have been interpreted to indicate an atmospheric O₂ concentration of less than 10⁻⁵ times the present level prior to the GOE (Pavlov and Kasting, 2002). Recent work has shown that such fractionations may be produced by interactions with organic carbon (Watanabe et al., 2009), but to a lesser degree than by atmospheric photochemistry. Evidence from sulfur isotopes (Kaufman et al., 2007; Ono et al., 2009a; Kendall et al., 2010), molybdenum isotopes (Wille et al., 2007; Duan et al., 2010; Voegelin et al., 2010), nitrogen isotopes (Garvin et al., 2009; Godfrey and Falkowski, 2009), chromium isotopes (Frei et al., 2009), and transition metal abundances (Anbar et al., 2007; Kendall et al., 2010) increasingly suggests a more complex oxidation history in the Archean and Paleoproterozoic than a single-step increase at the GOE [for a recent review, see Farquhar et al. (2011)]. Evidence from biomarkers (Brocks et al., 1999; Eigenbrode et al., 2008; Waldbauer et al., 2009) and carbon isotopes (Hayes, 1983; Eigenbrode and Freeman, 2006) suggest that both O₂ producers and consumers existed by ~2.7 Ga, although some of the early biomarker evidence has been recently questioned (Rashby et al., 2007; Rasmussen et al., 2008). Continued debates notwithstanding, *in toto*, these lines of evidence suggest a more complex atmospheric O₂ history in the Archean than previously thought.

Variations in concentrations and isotopic compositions of redox-sensitive transition metals such as iron and molybdenum can provide evidence for free O₂, although it has been difficult to quantify the amount of O₂ that was present in the surface environments of the ancient Earth. Oxidation of aqueous ferrous Fe [Fe(II)_{aq}] at circumneutral pH produces insoluble Fe(III) oxides, the largest inventory of which, in the Precambrian rock record, lies in banded iron formations (BIFs). Large BIFs that formed near the Archean–Proterozoic boundary have been proposed to indicate the presence of free O₂ in the atmosphere (Cloud, 1968), and experimental work has shown that a moderate concentration of O₂-producing photosynthesizers (perhaps less than 10% that of typical modern populations) could have produced sufficient O₂ to oxidize all of the Fe present in the BIFs of the Hamersley Province (Trouwborst et al., 2007). Alternatively, anoxygenic photosynthetic Fe(II)_{aq} oxidation (APIO) could also potentially explain these deposits (Konhauser et al., 2002; Kappler et al., 2005). Semi-quantitative estimates of free O₂ concentrations in the atmosphere have been made based on Fe retention in paleosols (Rye and Holland, 1998), but such calculations assume Fe immobility, which may not be valid (Yamaguchi et al., 2007). Iron isotope compositions of sedimentary rocks, including BIFs, shales, and carbonates, have been interpreted to record Fe oxidation in the late Archean (Rouxel et al., 2005; Anbar and Rouxel, 2007; Czaja et al., 2010). These data do not provide conclusive evidence for free O₂, however, because APIO can produce Fe isotope fractionations similar to those produced by abiological Fe

oxidation (Croal et al., 2004). Oxidation of Mo in continental sulfides and crystalline rock produces the soluble MoO₄²⁻ oxyanion that can enter the hydrosphere and become isotopically fractionated by redox reactions and sorption to Fe and Mn oxides (Siebert et al., 2003; Barling and Anbar, 2004; Tossell, 2005). Molybdenum isotope compositions of shales and carbonates have been used as proxies for the presence of O₂ in the Archean environment (Wille et al., 2007; Duan et al., 2010; Voegelin et al., 2010), but it has not been possible to constrain the quantity of free O₂ using Mo isotope compositions alone.

We propose that low-Fe Ca–Mg carbonates and black shales provide a proxy for the aqueous Fe and Mo isotope compositions of the Neoproterozoic Transvaal Basin of the Kaapvaal Craton in South Africa, and that these compositions were produced by oxidation of Fe(II)_{aq} by free O₂ and sorption of MoO₄²⁻ to the Fe(OH)₃ that was produced. The present paper provides quantitative constraints on O₂ contents of the surface waters of an Archean marine basin via coupled Fe and Mo isotope variations in Neoproterozoic carbonates and shales. Modeling of Fe oxidation by photosynthetically produced O₂, accompanied by Mo sorption, indicates the presence of free O₂ in the photic zone, and constrains the minimum concentration that is required to produce the measured isotopic compositions. These results demonstrate that the combination of Fe and Mo isotopes place important constraints on surface environmental conditions of the ancient Earth.

2. MATERIALS, METHODS, AND TRANSPORT MODEL

2.1. Samples and geologic setting

Thirty-five carbonate and 29 black shale samples from the Agouron–Griqualand Paleoproterozoic Drilling Project cores GKP01 and GKF01 were analyzed for their Fe isotope and mineral compositions. These cores were recovered from the Neoproterozoic–Paleoproterozoic Transvaal Supergroup in the southwest region of the Kaapvaal Craton in South Africa (Schröder et al., 2006; Knoll and Beukes, 2009). Samples were collected from the ~2.68 to 2.50 billion-year-old Ghaap Group, and were previously analyzed for Mo isotope compositions (carbonates: Voegelin et al., 2010; shales: Wille et al., 2007). Details of the geologic setting and drill core collection have been reported previously (Beukes, 1987; Schröder et al., 2006; Sumner and Beukes, 2006; Wille et al., 2007; Knoll and Beukes, 2009; Voegelin et al., 2010). Briefly, the cores were collected from two points on the craton, ~24 km apart, on the slope distal to the Campbellrand–Malmani carbonate platform; GKP01 preserves sediments from the deepest part of the slope, and GKF01 from further up slope, toward the platform (Schröder et al., 2006). These cores were collected to study the geological and geochemical properties of the platform-to-basin transition in this exquisitely preserved sedimentary sequence. Both sedimentological and geochemical evidence suggests that this basin was oxygenated down to a depth of several hundred meters, well below the photic zone (Beukes and Gutzmer, 2008; Kendall et al., 2010). The transition

from oxidized water at shallow depths to anoxic ferruginous water in the deep basin was likely not a sharp boundary, but rather a broad zone, the depth of which fluctuated based on the relative inputs of hydrothermally sourced aqueous Fe and photosynthetically derived O₂ (Beukes and Gutzmer, 2008).

2.2. Sample mineralogies and iron budgets

Traditionally, iron speciation and mineralogy in sedimentary rocks are determined by sequential extraction of powdered rock samples (e.g., Poulton and Canfield, 2005; Reinhard et al., 2009; Kendall et al., 2010). This technique, however, is typically performed on shales and carbonates that have moderate to high iron concentrations. The very low-Fe carbonates investigated in this study required a different approach, and so high resolution X-ray diffraction (XRD) patterns were used to quantify Fe mineralogies. Knowledge of the mineralogies of the carbonate samples was particularly important because molybdenum fractionation is influenced by the type of minerals into which Mo is incorporated or to which it is sorbed, specifically oxides and sulfides. The shale samples analyzed by Wille et al. (2007) for Mo isotope compositions had been ashed, so neither sequential extractions nor XRD analyses were performed for these samples, but Fe speciation data on similar samples from the same cores (Kendall et al., 2010) provide broad indications of the Fe mineralogy of shales in cores GKP01 and GKF01.

X-ray diffraction patterns were measured for all carbonate samples at the S.W. Bailey X-ray Diffraction Laboratory at the University of Wisconsin–Madison using a Rigaku Rapid II D/Max X-ray diffractometer using MoK α radiation, a system that is optimized for the detection of low abundance Fe phases. Each powdered sample was placed in a glass capillary tube and analyzed for 20 min under conditions of 50 kV and 50 mA using a 0.1 mm collimator. Patterns were acquired over a 2θ range of 2–44°, and were analyzed using JADE 9 software. No baseline subtractions were performed.

Because XRD is a novel technique for this type of study, the detection limits for Fe oxides and pyrite were tested using artificial samples made from powdered minerals. By weight, these samples were made from 0.1, 0.5, or 5 wt.% each of hematite, magnetite, and pyrite, and the remainder was composed of calcite. These samples were measured using the same conditions as those used for the Ghaap Group carbonate samples. [Electronic Annex Fig. EA-1-1](#) shows the XRD patterns of these test samples, and demonstrates that the detection limits for pyrite, magnetite, and hematite are between 0.1 and 0.5 wt.%.

Pyrite Fe abundances were calculated from comparison of XRD spectra of samples and test powders. The [311] reflection of pyrite was most useful in these calculations ($2\theta = 25.082^\circ$) because of the absence of interferences from reflections of other phases. The ratio of the intensity of this reflection to that of the [104] reflection of calcite in the 5 wt.% and 0.5 wt.% test samples was determined and used to calculate the abundance of pyrite in the natural samples. Care was taken to be sure that the reflection at $2\theta = 25.082^\circ$

in the samples was truly the [311] reflection of pyrite rather than that of another phase. This was accomplished by looking for evidence of other pyrite reflections ([200], [210], [211], and [220]). These were often partially obscured by other, more intense reflections of dolomite, but when present they could be seen as shoulders and therefore differentiated from the background.

2.3. Isotope analyses

Iron isotope compositions were determined on total and HCl partial digestions of carbonates, and of total digestions of shales. For details of procedures used to powder the carbonates and shales, see Voegelin et al. (2010) and Wille et al. (2007), respectively. For whole-rock Fe isotope analyses of carbonates, 5–50 mg of each powder was digested using concentrated HF and HNO₃ in a Savillex vial, followed by drying and further digestion in high-molarity HCl. A second aliquot of each carbonate sample powder was digested in a 15 mL centrifuge tube using 10 mL of 0.1 M HCl, a procedure designed to digest carbonates, but not any Fe-bearing crystalline oxides, sulfides, or silicates (Kostka and Luther, 1994; Severmann et al., 2004). The tubes were capped and shaken several times over the course of 24 h using a vortex mixer. Tubes were also periodically uncapped to reduce the $p\text{CO}_2$ in the headspace. After 24 h, the samples were centrifuged and the supernatant decanted into HCl-leached LDPE bottles. For all samples (whole-rock and partial digestions), iron contents were measured by the *Ferrozine* method (Stookey, 1970) after the dissolution step. An aliquot of each shale sample was dissolved using the same total digestion procedure as used for carbonates. However, prior to digestion, the shale samples were ashed at 850 °C overnight to remove the abundant organic matter in the shales.

Aliquots of all samples were purified twice by anion exchange chromatography using BioRad AG 1-X4 200–400 mesh resin, HCl, and standard techniques (Skulan et al., 2002; Beard et al., 2003a). Iron contents were remeasured by the *Ferrozine* method after chromatographic separation to check the Fe yields from the ion-exchange columns, all of which were greater than 90%, and most were greater than 95%.

Iron isotope compositions were measured by multi-collector, inductively-coupled plasma mass spectrometry (MC-ICP-MS; Micromass, *IsoProbe*) at the University of Wisconsin–Madison (Beard et al., 2003a; Albarède and Beard, 2004). In this study, Fe isotope compositions are defined as $\delta^{56}\text{Fe} = [({}^{56}\text{Fe}/{}^{54}\text{Fe})_{\text{sample}}/({}^{56}\text{Fe}/{}^{54}\text{Fe})_{\text{standard}} - 1] \times 1000$ and $\delta^{57}\text{Fe} = [({}^{57}\text{Fe}/{}^{54}\text{Fe})_{\text{sample}}/({}^{57}\text{Fe}/{}^{54}\text{Fe})_{\text{standard}} - 1] \times 1000$, both in units of per mil (‰), and are reported relative to the average of igneous rocks. The international standard IRMM-014 has a $\delta^{56}\text{Fe}$ value of -0.09‰ on this scale. The overall external precision of the Fe isotope analyses, based on multiple analyses of standards over the course of the analytical sessions, was 0.06‰ (2 standard deviations).

Samples were analyzed on multiple days and accuracy was checked using multiple standards (IRMM-014 and two lab standards, J-M Fe and HPS Fe) and nine test

solutions. Five of these test solutions were made by collecting the acid used to separate the rest of the elements from Fe on the anion-exchange columns (four represented typical carbonate samples and one represented a shale sample), and the other four were artificial solutions made from high-purity elemental standards. All solutions were amended with a measured quantity of Fe of known isotopic composition (HPS Fe, $\delta^{56}\text{Fe} = 0.49\text{‰}$) and processed through the entire purification protocol. These nine test solutions have an average $\delta^{56}\text{Fe}$ value of $0.51 \pm 0.06\text{‰}$ (2 standard deviations), which is identical to the pure HPS Fe within uncertainty.

In this study, Mo isotope compositions are defined as $\delta^{98}\text{Mo} = [({}^{98}\text{Mo}/{}^{95}\text{Mo})_{\text{Sample}}/({}^{98}\text{Mo}/{}^{95}\text{Mo})_{\text{Standard}} - 1] \times 1000$, in units of per mil (‰). The reference is an in-house standard solution (Johnson Matthey, 1000 $\mu\text{g}/\text{mL}$ ($\pm 0.3\%$) ICP standard solution, lot 602332B; Wille et al., 2007; Voegelin et al., 2010). See Voegelin et al. (2010) and Wille et al. (2007) for details of Mo isotope analyses. On this scale, the $\delta^{98}\text{Mo}$ value of modern open ocean water is $2.3 \pm 0.1\text{‰}$ (2 standard deviations; Siebert et al., 2003).

2.4. Fe–Mo transport and fractionation model

A one-dimensional dispersion/reaction model was developed to predict the Fe and Mo fluxes and attendant isotopic fractionations expected in a Neoproterozoic marine basin. In the model, free O_2 produced in the photic zone via oxygenic photosynthesis is transported downward by eddy diffusion to react with aqueous ferrous Fe [$\text{Fe}(\text{II})_{\text{aq}}$] transported upward from Fe(II)-rich (relatively) deep anoxic water, which produces oxidized ferric Fe oxide/hydroxide precipitates [$\text{Fe}(\text{OH})_3$]. Aqueous Mo (MoO_4^{2-}) from continental runoff sorbs to $\text{Fe}(\text{OH})_3$ particles and both settle out of the water column. The model allows exploration of the effects of varying the rate of O_2 production and concentrations of $\text{Fe}(\text{II})_{\text{aq}}$ and MoO_4^{2-} on the Fe and Mo isotope compositions of seawater as a function of water column depth. Because extensive Fe deposition occurred distally during deposition of the more proximal Ghaap Group carbonates and shales, and because there is no evidence for extensive Mn oxide deposition at this time (Beukes and Gutzmer, 2008), the dispersion/reaction model assumes that the major component of Mo sorption is to Fe(III) oxy/hydroxides.

Although the precise depth of the Transvaal Basin is not known, sedimentary features and sequence stratigraphy indicate that the basin deepened over the 150-million-year time span in which the sediments analyzed were deposited, to a maximum depth of at least several hundred to one thousand meters at the maximum stages of transgression (Beukes and Gutzmer, 2008). Thus, oxidation of $\text{Fe}(\text{II})_{\text{aq}}$ and removal of $\text{Fe}(\text{OH})_3$ and sorbed MoO_4^{2-} via settling were assumed to take place over a depth interval of 500 m to simulate conditions in deep Archean basins.

Dispersive transport was modeled using central finite-difference methods, as detailed in Boudreau (1997), using an eddy diffusion coefficient of $0.1 \text{ cm}^2 \text{ s}^{-1}$ based on values for the modern upper ocean (Ledwell et al., 1993, cited in Kappler et al., 2005). The upper (sea surface) boundary condition for O_2 was fixed at a value equal to that of seawater

Table 1
Fe–Mo– O_2 dispersion/reaction model parameters.

Parameter	Value
<i>Fe, Mo, O_2 transport parameters</i>	
Water depth	500 m
Eddy diffusion coefficient	$0.1 \text{ cm}^2 \text{ s}^{-1}$ ^a
Boundary conditions for O_2	
Upper	$2.52 \times 10^{-9} \mu\text{mol L}^{-1\text{b}}$
Lower	Zero-gradient
Boundary conditions for $\text{Fe}(\text{II})_{\text{aq}}$	
Upper	Zero-gradient
Lower	$100 \mu\text{mol L}^{-1}$
Boundary conditions for MoO_4^{2-}	
upper	$0.001 \mu\text{mol L}^{-1}$
lower	Zero-gradient
Rate of O_2 release ($R_{\text{O}_2\text{-rel}}$) (% of modern O_2 production)	$1.2 \times 10^{-8} \text{ mol dm}^{-3} \text{ day}^{-1}$ (2%) ^c
Photic zone depth range	0–100 m
Temperature	25 °C
Salinity	35 ppt
pH	7.8 ^d
$\text{Fe}(\text{OH})_3$ settling rate constant	$0.79 \text{ day}^{-1\text{e}}$
Simulation time	2000 years
<i>Isotopic fractionation parameters</i>	
Initial $\delta^{56}\text{Fe}$ ($\delta^{56}\text{Fe}_{\text{Fe}(\text{II})_{\text{aq}}-i}$)	0.0‰ ^f
Initial $\delta^{98}\text{Mo}$ ($\delta^{98}\text{Mo}_{\text{Mo-aq}-i}$)	0.2‰ ^g
$\alpha_{\text{Fe}(\text{OH})_3\text{-Fe}(\text{II})_{\text{aq}}}$	1.004^{h}
$\alpha_{\text{Mo}_{\text{sorb}}\text{-MoO}_4^{2-}}$	0.997^{h}
Coefficient of Mo sorption	2.20×10^{-6}
Rate constants for Fe and Mo isotope exchange	10^{13} day^{-1}

^a Ledwell et al. (1993).

^b In equilibrium with an atmospheric O_2 concentration of 10^{-5} PAL.

^c Modern global average rate of primary production = $0.06 \text{ mol m}^{-2} \text{ day}^{-1}$ (Riley and Chester, 1971).

^d Beukes and Gutzmer (2008).

^e Pizarro et al. (1995) and Taillefert and Gaillard (2002).

^f Beard et al. (2003b) and Johnson et al. (2008b).

^g See Section 4.1 for details and Voegelin et al. (2010).

^h See Section 4.1 for details.

in equilibrium with an atmospheric O_2 concentration of 10^{-5} PAL, the assumed maximum content of the Archean atmosphere based on mass-independent fractionation of sulfur (Pavlov and Kasting, 2002). A zero-gradient boundary condition was assumed for O_2 at the lower end of the spatial domain. For $\text{Fe}(\text{II})_{\text{aq}}$, a zero-gradient boundary condition was assumed for the upper boundary and the lower boundary was fixed at $100 \mu\text{mol L}^{-1}$, and for MoO_4^{2-} , a zero-gradient boundary condition was assumed for the lower boundary, and the upper boundary was fixed at $0.001 \mu\text{mol L}^{-1}$ (see Table 1 and Section 4.1 for details). It should be noted that the depth at which Fe oxidation occurred was not fixed in the model, but rather was allowed to evolve to a steady-state value based on the $\text{Fe}(\text{II})_{\text{aq}}$ boundary conditions and rates of O_2 release, as well as rates of eddy diffusion and Fe(II) oxidation.

The rate of O_2 release through photosynthesis ($R_{\text{O}_2\text{-rel}}$) was set to 2% of the modern global average rate of net

primary production of $0.06 \text{ mol m}^{-2} \text{ day}^{-1}$, based on the global average of $0.75 \text{ g C m}^{-2} \text{ day}^{-1}$ (values range from ~ 0.5 to $1 \text{ g m}^{-2} \text{ day}^{-1}$; Riley and Chester, 1971). Rates of O_2 release were set lower than net primary production to account for loss of O_2 through microbial respiration and oxidative degradation of organic matter, which consumes all but a few percent of photosynthetic O_2 production in the modern ocean (Schlesinger, 1997). For modeling, the areal rate was converted to a volumetric rate ($1.2 \times 10^{-8} \text{ mol dm}^{-3} \text{ day}^{-1}$), assuming the 100-m-thick photic zone as adopted in the simulations.

The rate of reaction between $\text{Fe(II)}_{\text{aq}}$ and O_2 was modeled using the temperature-, salinity-, and pH-dependent second-order rate law of Millero et al. (1987), assuming a temperature of $25 \text{ }^\circ\text{C}$, a salinity of 35‰, and a pH of 7.8. Model runs in which the seawater temperature was varied between 0 and $35 \text{ }^\circ\text{C}$ produced identical results. Although the pH of the Archean ocean is unknown, Beukes and Gutzmer (2008) argued that the pH of the Neoproterozoic Transvaal Basin had to be at least 7.8, the lower limit for carbonate precipitation. Reasonable changes to this value (± 1 pH unit) did not significantly alter the results of the modeling. Oxidized Fe was assumed to be converted immediately to Fe(OH)_3 particles. A rate constant of 0.79 day^{-1} was assumed for settling of Fe(OH)_3 particles based on experimentally-determined settling rates (Pizarro et al., 1995, cited in Taillefer and Gaillard, 2002). Increasing or decreasing this value by an order of magnitude did not significantly alter the model results.

The coupled dispersion/reaction equations were discretized at 2 m intervals (250 node points) and solved via the numerical method of lines (Boudreau, 1997) using the stiff ODE solver VODE (Brown et al., 1989), taking advantage of the banded Jacobian matrix that arises during solution of one-dimensional transport/reaction problems. A simulation time of 2000 years was employed, over which time the transport/reaction system achieved a dynamic steady-state condition.

The Fe isotope compositions of $\text{Fe(II)}_{\text{aq}}$ and Fe(OH)_3 , and the Mo isotope compositions of aqueous MoO_4^{2-} and Mo_{sorb} were computed by tracking the transport and reaction of these four species and the heavy (^{56}Fe or ^{98}Mo) and light (^{54}Fe or ^{95}Mo) isotopes of these phases, following the methods described in Walker (1991). Equilibrium $^{56}\text{Fe}/^{54}\text{Fe}$ and $^{98}\text{Mo}/^{95}\text{Mo}$ isotope exchange between Fe(OH)_3 and $\text{Fe(II)}_{\text{aq}}$, and between Mo_{sorb} and MoO_4^{2-} , respectively, was simulated using two opposite-direction kinetic equations (Criss, 1999), using fractionation factors for Fe oxide precipitation and Mo sorption to Fe oxides (Table 1), as well as rate constants high enough (10^{13} day^{-1}) to reproduce near-instantaneous exchange. Sorption of Mo to Fe(OH)_3 was modeled using an isotherm derived from the study of Goldberg et al. (2009).

3. RESULTS

3.1. Sample mineralogy

Twenty-nine of the 35 carbonate samples analyzed here are composed of ferroan dolomite, with or without minor

quartz and other clastic materials (Electronic Annex Fig. EA-1-2). Ferroan dolomite was identified using XRD patterns by noting the shift of the [104] reflection toward values lower than those for pure dolomite at a 2θ angle of 14.10° . The other six samples (from the Vryburg Formation of core GKP01, and the Lokammona and Monteville formations of core GKF01) are composed of calcite or calcite plus ankerite, together with clastic material.

The dominant mineralogy of each carbonate sample is summarized in Electronic Annex Table EA-2-2 and is shown schematically in Fig. 1a. No Fe oxides were detected in any of these samples above the detection limit of $\sim 0.1 \text{ wt.}\%$, but fifteen samples contain minor, but detectable pyrite (Table EA-2-2, Fig. EA-1-2). In twelve of these latter samples, pyrite Fe (Fe_{pyr}) was calculated to account for $\sim 30\%$ or less of the total Fe (Fe_T), although most have considerably less. In the other three samples, pyrite Fe was calculated to represent $\sim 50\%$ of the total Fe. The measured carbonate Fe contents (Fe_{carb}), as determined by HCl extraction, however, account for 75–99% of the Fe in each of these three samples. The apparent discrepancy in the Fe measurements is likely due to an overestimate of the pyrite content because of the small amount of Fe_T in these samples and the resulting uncertainty in the measurement of small peak heights in the XRD patterns. The low levels of Mo in these carbonates ($\leq 1 \text{ ppm}$; Table EA-2-2) makes it difficult to determine the phase in which Mo resides, but the absence of Fe oxides in these samples, and a lack of correlation between Mo and pyrite abundances (Fig. EA-1-3), or between Mo and total Fe abundances (Voegelin et al., 2010), indicates that Mo is most likely directly incorporated into the carbonate lattice, rather than in any included oxides or sulfides. In summary, the samples are composed almost entirely of Fe- and Mo-bearing carbonate, with no detectable Fe-oxides, and pyrite is at most a minor component in less than half of the samples analyzed. The Fe and Mo isotope compositions measured in the carbonates are therefore inferred to reflect those of the carbonates, which in turn potentially allow a direct connection to be made to the Fe and Mo isotope compositions of seawater in the Neoproterozoic Transvaal Basin.

The shales studied here contain various proportions of clastics and carbonate, based on whole-rock geochemical data, including losses on ignition (LOI) (Table EA-2-3), as well as other samples collected from the same cores (Schröder et al., 2006; Fig. EA-1-4 of this study). Based on the range of S contents for shales from cores GKP01 and GKF01 (Schröder et al., 2006), pyrite comprises a significant portion of the Fe budget of many of these samples (Fig. EA-1-4). The balance of the Fe budget is likely to be contained in Fe carbonates, Fe oxides, and Fe silicates. As is common with most shales, the Mo budget is likely dominated by organic carbon and sulfides (Wille et al., 2007).

3.2. Fe and Mo isotope compositions and elemental concentrations

All but one of the carbonate Fe samples have negative $\delta^{56}\text{Fe}$ values that range from -3.69‰ to -0.07‰ , as determined by HCl extractions (Fig. 1b and Electronic Annex

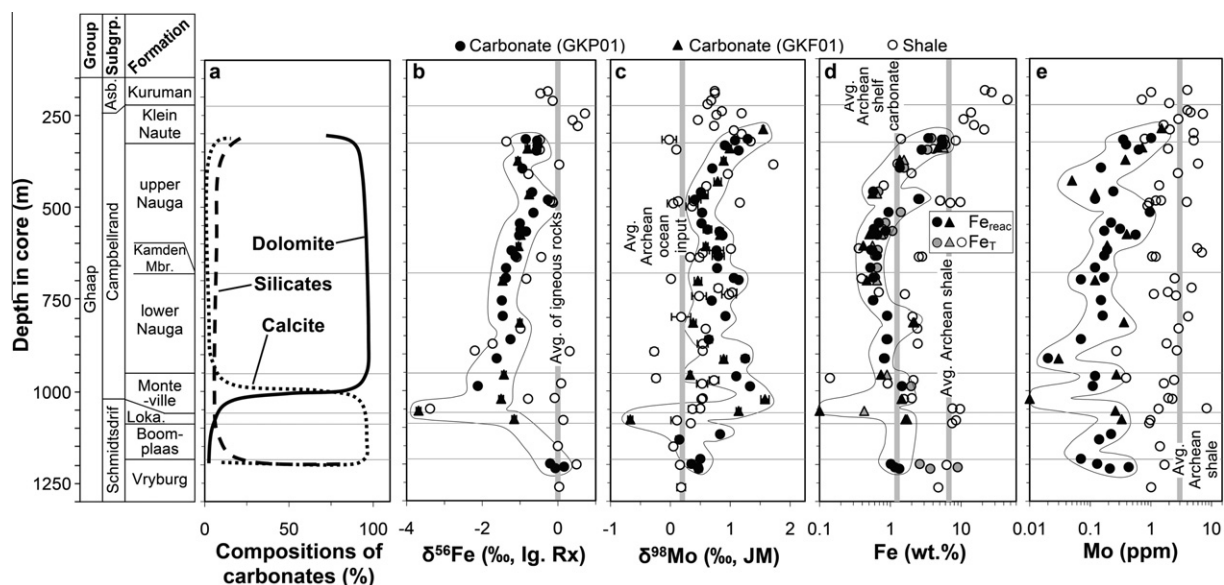


Fig. 1. Mineralogy, Fe and Mo isotope compositions, and Fe and Mo contents of Neoproterozoic carbonates and shales from drill cores GKP01 and GKF01 of the Ghaap Group, South Africa, plotted against stratigraphy. Data from core GKF01 have been projected onto those of core GKP01, based on inter-core stratigraphic correlations (Schröder et al., 2006; Knoll and Beukes, 2009). (a) Percentages of dolomite, calcite, and silicates (a majority of which are quartz with minor chamosite and muscovite) in each sample based on XRD data presented in Fig. EA-1-2. Traces have been redrawn schematically with a smoothed line for ease of viewing. Parts (b–e) present isotopic and geochemical data for carbonates (filled symbols, outlined) and shales (open symbols). (b) Fe isotope data (see Tables EA-2-1 and EA-2-2 and EA-2-3). The vertical gray bar ($\delta^{56}\text{Fe} = 0\text{‰}$) represents the average crustal rock and average Archean hydrothermal Fe $\delta^{56}\text{Fe}$ values. (c) $\delta^{98}\text{Mo}$ values for carbonates and shales from Voegelin et al. (2010) and Wille et al. (2007), respectively. See also Tables EA-2-2 and EA-2-3. The vertical gray bar represents the Mo isotope composition of the continental input to the Neoproterozoic ocean (see text for details). (d) Fe contents (see Tables EA-2-2 and EA-2-3). For the carbonate samples, black symbols represent reactive Fe extracted using 0.1 M HCl (Fe_{reac}), and gray symbols represent total Fe (Fe_{T}) (Table EA-2-2). The data from shales are Fe_{T} contents (Table EA-2-3). The vertical gray bars represent average total Fe contents of Archean shelf carbonates ($\text{Fe}_{\text{T}} = 1.24$ wt.%; Veizer et al., 1990) and Archean shales ($\text{Fe}_{\text{T}} = 6.72$ wt.%; Taylor and McLennan, 1985). (e) Mo contents of carbonates and shales from Voegelin et al. (2010) and Wille et al. (2007), respectively. See also Tables EA-2-2 and EA-2-3. The vertical gray bar represents the average Mo content of Archean shales (Yamaguchi, 2002). The error bars for $\delta^{56}\text{Fe}$ values represent ± 2 standard deviations of multiple analyses of our test solutions ($\pm 0.06\text{‰}$; Section 2.3 and Table EA-2-1), and are smaller than the size of the symbols. The error bars for $\delta^{98}\text{Mo}$ values represent ± 2 standard deviations (Wille et al., 2007; Voegelin et al., 2010; Tables EA-2-2 and EA-2-3). Abbreviations: Asb., Asbesheuwels; Loka., Lokamma; Mbr., Member; Subgrp., Supergroup.

Table EA-2-1). The Fe isotope compositions of the whole-rock carbonate digestions are virtually identical to those of the corresponding HCl digestions for almost all samples (Tables EA-2-1 and EA-2-2), confirming that the measured Fe isotope compositions reflect those of the carbonates, and that the effects of mineral inclusions are insignificant. The $\delta^{56}\text{Fe}$ values of the bulk shales from the section define a similar range as that of the carbonates, from -3.38‰ to $+0.71\text{‰}$ (Fig. 1b and Table EA-2-1). All but one of the $\delta^{98}\text{Mo}$ values of the carbonate samples are positive, and range from $+0.15\text{‰}$ to $+1.58\text{‰}$ (Voegelin et al., 2010; Fig. 1c and Table EA-2-2 of this study). The $\delta^{98}\text{Mo}$ values of the bulk shales from the section range from -0.27‰ to $+1.72\text{‰}$ (Wille et al., 2007; Fig. 1c and Table EA-2-3 of this study). The range of $\delta^{56}\text{Fe}$ and $\delta^{98}\text{Mo}$ values of the carbonates in cores GKP01 and GKF01 are similar to each other (Fig. 1 and Table EA-2-2).

The carbonates analyzed here have very similar total Fe (Fe_{T}) and reactive Fe (Fe_{reac}) contents (Fig. 1d), which confirms that the measured Fe isotope composition reflect Fe in the carbonate lattice and not other minerals. The Fe_{reac} contents of the carbonates also matches well those of previ-

ously reported Archean shelf carbonates ($\text{Fe}_{\text{T}} = 1.24$ wt.%; Veizer et al., 1990), except those in the uppermost Nauga Formation and Klein Naute Formation, which have relatively high Fe contents, marking the transition to BIF deposition upward in the sequence. The Fe_{T} contents of the shales are more variable than those of the carbonates (Fig. 1d), and, importantly, most of them are significantly lower than the average of Archean shales ($\text{Fe}_{\text{T}} = 6.72$ wt.%; Taylor and McLennan, 1985). The relatively low Fe_{T} contents of the shales in the lower and middle parts of the stratigraphic section follow the trends observed in the carbonates. The shales in the uppermost Nauga and Klein Naute formations have Fe_{T} contents that are relatively higher than those lower in the section, also following the trends seen in the carbonates, accompanying the transition to BIF deposition. Total Fe contents of shales in the Kuruman Iron Formation are high. The Mo contents of the carbonates are variable and show no clear stratigraphic trend (Fig. 1e). The Mo contents of the shales analyzed here are also somewhat variable and generally an order of magnitude greater than those of the carbonates. The relatively high Mo contents of the shales are similar, however, to

the average of previously measured Archean shales (Yamaguchi, 2002).

4. DISCUSSION

4.1. Fe and Mo concentrations and fluxes in the Archean ocean

A review of Fe and Mo cycles in the Neoproterozoic oceans is required before discussing the results of the dispersion/reaction modeling, as well as the implications for Fe and Mo isotope variations in the rocks studied. Previous estimates for the aqueous Fe content of the Archean oceans have largely relied on study of BIFs (e.g., Holland, 1984). Deposition of the Ghaap Group carbonates and shales studied here was contemporaneous with deposition of iron formation in deeper offshore waters (Beukes, 1987; Beukes and Gutzmer, 2008). Because of the close correlations that have been made between the Kaapvaal and Pilbara cratons, which indicate that the Hamersley and Transvaal basins were likely connected (e.g., Beukes and Gutzmer, 2008), we can turn to iron formations of the Pilbara Craton, which have excellent geochronological constraints, to constrain Fe fluxes at the time of deposition of the Ghaap Group samples. The Fe contents required to produce the Hamersley Province BIFs range from a few tens to roughly one thousand μM (e.g., Ewers, 1980; Morris and Horwitz, 1983; Holland, 1984). Although these estimates are largely based on deposition of the Brockman Iron Formation, a unit that post-dates those studied here, we suggest that a relatively conservative estimate for the $\text{Fe(II)}_{\text{aq}}$ concentration of the deep ocean at this time is 100 to several hundred μM , and the lower end of this range formed the initial input of the dispersion/reaction model.

The Mo content of the Archean ocean is also poorly constrained, largely because of the lack of knowledge of the O_2 content of the atmosphere at the time, which is the main factor that determines the Mo weathering flux to the oceans. Oxidation of continental sulfides is thought to be the main source of Mo to the modern ocean (Anbar et al., 2007), and sorption of Mo to Fe–Mn oxides is quantitatively the most important sink in modern marine environments (Barling et al., 2001; Siebert et al., 2003; Barling and Anbar, 2004). However, prior to the increase in marine sulfate contents and subsequent sequestration of sulfides in sedimentary rocks that occurred after the GOE, continental sources of Mo were likely dominated by relatively low-Mo crystalline silicate rocks (Farquhar et al., 2011). Although the solubility of such rocks in an atmosphere that has an O_2 partial pressure less than 10^{-5} PAL is not known, because the low- O_2 Archean atmosphere was maintained in part by oxidation of reduced continental rocks, at least some Mo is expected to have been oxidized and released to the ocean from the continents. The other main source of Mo to the modern ocean is low-temperature hydrothermal systems (McManus et al., 2002). Although this source only accounts for $\sim 13\%$ of the Mo flux to the modern ocean (McManus et al., 2002), it has been proposed that with less continental weathering, this flux would have been quantitatively more important in the Archean. In the

modern ocean, the hydrothermal Mo flux is produced by interactions of seawater with basaltic rocks at ridge systems. In the Archean, the anoxic bottom water interacting with such rocks would likely not have produced significant soluble MoO_4^{2-} , suggesting that continental sources may still have dominated the marine Mo budget. It has been suggested, based on Mo/TOC (total organic carbon) ratios (Duan et al., 2010), that the Mo content of the Archean ocean was probably no more than $0.001 \mu\text{M}$ ($\sim 1\%$ of the modern value of $0.11 \mu\text{M}$; Collier, 1985), and this value was used as the initial input for the dispersion/reaction model.

The Fe isotope compositions of Fe sources to the ancient ocean are relatively well constrained. Johnson et al. (2008b) reviewed the isotopic compositions of these sources and argued that an $\text{Fe(II)}_{\text{aq}}$ -rich ocean would likely have an average $\delta^{56}\text{Fe}$ value near 0‰ , because the mass-weighted hydrothermal input lies close to the average of igneous rocks, and bulk detritus from riverine fluxes were also close to the average of igneous rocks. Hydrothermal Fe in the modern Earth has an average mass-weighted $\delta^{56}\text{Fe}$ value of $\sim -0.2\text{‰}$, but the higher heat flow in the Archean would have resulted in less fractionation during hydrothermal leaching of Fe from the crust and a $\delta^{56}\text{Fe}$ value closer to 0‰ (Johnson et al., 2008a). We therefore take the Fe fluxes to the Archean oceans to have had a $\delta^{56}\text{Fe}$ value of 0‰ , and this forms the input value in the dispersion/reaction model.

The average Mo isotope compositions of Mo sources to the ancient ocean are not as well constrained as that of Fe, and have likely varied over Earth's history. The Mo isotope composition of riverine MoO_4^{2-} , the primary source of Mo to the modern ocean, ranges from a $\delta^{98}\text{Mo}$ value of 0.2‰ to 2.4‰ , and has a weighted average $\delta^{98}\text{Mo}$ value of 0.7‰ (Archer and Vance, 2008). There is, however, no *a priori* reason to assume that the $\delta^{98}\text{Mo}$ value has been constant throughout time, particularly in Archean environments, which were less oxygenated than today. The Mo isotope compositions measured from modern river water are a consequence of variations in the isotopic compositions of source rocks (Neubert et al., 2008b, 2011), and fractionation processes, such as sorption of dissolved MoO_4^{2-} to Fe and Mn oxides and clay minerals during weathering (Archer and Vance, 2008). Concerning source rock variation, Pearce et al. (2010) analyzed numerous catchments that drain a homogeneous bedrock (basalt) in Iceland and concluded that the Mo isotope compositions of rivers that have Mo budgets dominated by physical weathering (and/or enhanced silicate weathering at low pH) are not distinguishable from those of continental silicate rocks, which have $\delta^{98}\text{Mo}$ values of $\sim 0\text{‰}$. Therefore, in the absence of significant soil formation, as was likely the situation in the Late Archean, isotopic fractionation due to chemical weathering would be expected to be less significant than today. Concerning variable fractionation processes, some young sediments have Mo isotope compositions that vary significantly from those of silicate rocks, and have measured $\delta^{98}\text{Mo}$ values up to 2.3‰ (Neubert et al., 2008a). Consistent with this, Neubert et al. (2011) demonstrated that erosion of such marine sedimentary rocks is a source of isotopically

heavy Mo to the dissolved river load. These marine sediment values, however, are produced under present oxidizing conditions, and require significant Mo sequestration in oxic environments (Siebert et al., 2003); therefore, such rocks and isotopic compositions do not represent an analog for weathering of bedrock exposed to Late Archean rivers.

In contrast, weathering of Mo-bearing sulfides in crystalline rocks by the small amount of O₂ in the pre-GOE atmosphere would have made a significant contribution to the Mo flux to the ocean. Published $\delta^{98}\text{Mo}$ values of MoS₂ vary widely over a few per mil, but the average $\delta^{98}\text{Mo}$ value is 0.4‰ (Greber et al., 2011). Further evidence for the Mo composition of the Archean ocean is provided by the Mo isotope compositions of shale samples from the 3.2 Ga Fig Tree Group. These shales, which were likely deposited under anoxic conditions and therefore involved little to no oxide-related isotopic fractionation, have an average $\delta^{98}\text{Mo}$ value of 0.2‰ (Wille et al., 2007). The average $\delta^{98}\text{Mo}$ value of the Archean ocean input was, therefore, likely between 0.2‰ and 0.4‰. We assume a conservative average $\delta^{98}\text{Mo}$ value of 0.2‰ for the sources of Mo to the Archean ocean, and this is the input value in the dispersion/reaction model. An increase in the isotopic composition of the initial Mo input in the dispersion/reaction model to a $\delta^{98}\text{Mo}$ value of 0.4‰ from 0.2‰ simply increases the output $\delta^{98}\text{Mo}$ value by 0.2‰.

The isotopic fractionation factors used are estimates based on those determined in experimental studies. The average ⁵⁶Fe/⁵⁴Fe fractionation factor between aqueous Fe(II) and Fe(III) oxide/hydroxides ($\alpha_{\text{Fe}(\text{OH})_3-\text{Fe}(\text{II})_{\text{aq}}}$) that has been experimentally determined under conditions most similar to the Archean ocean (including high silica content) has a value of 1.0032, but the highest value measured is 1.0040 (Wu et al., 2011); we use the higher value here to illustrate the maximum Fe isotope fractionation. The published ⁹⁸Mo/⁹⁵Mo isotope fractionation factor for Mo sorption to ferrihydrite ($\alpha_{\text{Mo}_{\text{sorb}}-\text{MoO}_4^{2-}} = 0.999$) was experimentally determined under conditions rather dissimilar to the Archean ocean (Goldberg et al., 2009), and thus may not be appropriate, other than to indicate the direction of fractionation. It is possible, for example, that the presence of dissolved Si in the Precambrian oceans influences the Mo isotope fractionation factor, as it does for $\alpha_{\text{Fe}(\text{OH})_3-\text{Fe}(\text{II})_{\text{aq}}}$, which can vary by 2‰ (Wu et al., 2011), although this remains unknown. We illustrate the Mo isotope fractionations produced by sorption to Fe(III) oxide/hydroxides by use of $\alpha_{\text{Mo}_{\text{sorb}}-\text{MoO}_4^{2-}} = 0.999$ and 0.997 to accommodate possible ranges in fractionation factors.

We assume that the small pools of residual Fe(II)_{aq} and MoO₄²⁻ in the coupled Fe–Mo isotope fractionation model are directly incorporated into the carbonates without any isotopic fractionation. The low Fe contents of the majority of these samples (<1 wt.%; Fig. 1) suggest that incorporation may have been quantitative, leading to no net Fe isotope fractionation. Based on the Fe(II)_{aq}–siderite fractionation factor of +0.5‰ measured for ⁵⁶Fe/⁵⁴Fe by Wiesli et al. (2004), equilibrium partitioning of Fe isotopes between aqueous Fe and carbonate would shift our model results to lower $\delta^{56}\text{Fe}$ values for carbonate. Our assumption of quantitative sequestration of aqueous Fe(II) into

carbonate, however, produces maximum predicted $\delta^{56}\text{Fe}$ values for carbonate. The use of carbonates as a proxy for the Mo isotope composition of seawater is a relatively recent innovation and further work is certainly warranted, but we accept the evidence at hand that incorporation of Mo into marine non-skeletal carbonates proceeds without isotopic fractionation (Voegelin et al., 2009).

The Mo isotope compositions of shales are controlled by the degree of scavenging by sulfide minerals. It has been suggested that below a critical H₂S_{aq} concentration of 11 μM, this scavenging is incomplete, which leads to fractionation of the residual Mo (Helz et al., 1996; Erickson and Helz, 2000; Neubert et al., 2008a; Nägler et al., 2011). Further recent work has shown that Mo isotope fractionation associated with incorporation into sulfides may be more complex, and additionally is dependent on pH and availability of reactive Fe species (Helz et al., 2011). Thus, the use of Mo isotope compositions of shales as seawater proxies may be dependent on H₂S_{aq} content, pH, and reactive Fe contents, and these geochemical conditions may vary over time within a basin. In addition, the Fe and Mo isotope compositions of shales may include seawater and clastic components. Collectively, these issues generally indicate that the maximum $\delta^{98}\text{Mo}$ values measured in shales records the minimum values of seawater (Wille et al., 2007), whereas the minimum $\delta^{56}\text{Fe}$ values of the shales probably reflect the maximum $\delta^{56}\text{Fe}$ values of seawater. The rough covariation of $\delta^{56}\text{Fe}$ and of $\delta^{98}\text{Mo}$ data from carbonates and shales in these cores (Fig. 1) supports the proposal that they each record a dominantly seawater signal (Wille et al., 2007; Voegelin et al., 2010).

4.2. Fe–Mo isotope variations in the Ghaap Group

The near-zero $\delta^{56}\text{Fe}$ values and slightly positive $\delta^{98}\text{Mo}$ values of the shallow water samples from the siliciclastic-rich Vryburg, Boomplaas, and Lokamma formations (Fig. 1) may reflect a dominantly continental input, but it is also important to note that these units formed in shallower water early in the history of the basin (Schröder et al., 2006; Beukes and Gutzmer, 2008) and likely had a different authigenic history than the overlying samples. The shift to lower $\delta^{56}\text{Fe}$ and higher $\delta^{98}\text{Mo}$ up section is interpreted to reflect a largely seawater component. In the carbonates, up section, $\delta^{56}\text{Fe}$ values initially decrease and then increase, a trend that is roughly mirrored by the $\delta^{98}\text{Mo}$ values in the same carbonates, which initially increase and then decrease slightly upward toward the transition to the Kuruman Iron Formation. The $\delta^{56}\text{Fe}$ and $\delta^{98}\text{Mo}$ values of the shales analyzed here show more scatter through the section than those of the carbonates, reflecting the complexities discussed above, including variable clastic contributions, but the $\delta^{56}\text{Fe}$ values are generally negative and the $\delta^{98}\text{Mo}$ values are generally positive, the latter increasing in scatter up section (Fig. 1). Up to the Kuruman IF, Fe contents increase, and $\delta^{56}\text{Fe}$ values are moderately negative and $\delta^{98}\text{Mo}$ values increase (Fig. 1). Iron and Mo isotope compositions in the section studied are therefore broadly anti-correlated, where negative $\delta^{56}\text{Fe}$ values are associated with positive $\delta^{98}\text{Mo}$ values.

We suggest that the only plausible mechanism for simultaneously producing a decrease in $\delta^{56}\text{Fe}$ values for seawater $\text{Fe(II)}_{\text{aq}}$ and an increase in $\delta^{98}\text{Mo}$ values for seawater MoO_4^{2-} is through coupled formation of Fe(III) oxide/hydroxides [Fe(OH)_3] and sorption of dissolved MoO_4^{2-} , the process that was simulated in the dispersion/reaction model (Section 2.4). Conceptual pathways for covariation in Fe and Mo isotope compositions in Archean seawater are shown in Fig. 2. As precipitation of Fe(OH)_3 proceeds, the initially very small, isotopically heavy Fe(OH)_3 and light Mo_{sorb} pools increase in size and their isotopic compositions trend toward the initial values, while the decreasing amounts of residual $\text{Fe(II)}_{\text{aq}}$ and MoO_4^{2-} in seawater become isotopically lighter and heavier, respectively. It is important to emphasize that it is these residual pools of Fe and Mo that are incorporated into the analyzed carbonates, comprising the seawater proxy.

Sequestration of Fe and Mo into sedimentary sulfides is another potential control on Fe and Mo budgets. Sulfide control of the Fe and Mo isotope compositions in the Ghaap Group could occur through sulfide precipitation and sequestration elsewhere in the basin, or in interbedded sulfide-bearing shales, which could have left behind residual $\text{Fe(II)}_{\text{aq}}$ and MoO_4^{2-} pools analogous to the Fe oxide precipitation model described above (Fig. 2). The nature of Fe isotope fractionation during sedimentary sulfide production is still somewhat uncertain. Many low-temperature sedimentary sulfides of Neoproterozoic and Paleoproterozoic ages have negative $\delta^{56}\text{Fe}$ values (Johnson et al., 2008b), and Guilbaud et al. (2011) propose that abiogenic pyrite formation from FeS precursors can produce low- $\delta^{56}\text{Fe}$ pyrite, although it is important to stress that the Guilbaud et al. (2011) model only produces a few percent pyrite that has highly negative $\delta^{56}\text{Fe}$ values relative to the initial Fe inventory. If such low- $\delta^{56}\text{Fe}$ pyrite controlled the Fe budget of the analyzed carbonates, this might explain the data, but, as noted above, the Fe budgets of the carbonates generally contain only a small contribution from pyrite. Precipitation of low- $\delta^{56}\text{Fe}$ pyrite elsewhere in the basin, or in interbedded shales, would produce positive $\delta^{56}\text{Fe}$ values in seawater $\text{Fe(II)}_{\text{aq}}$ that would be sequestered in carbonate (Fig. 2), but this is opposite to what is observed, indicating this model is unlikely. Alternatively, equilibrium precipitation of pyrite, using the predicted fractionation factors of Polyakov and Sultantov (2011), would produce pyrite that has positive $\delta^{56}\text{Fe}$ values, which would produce negative $\delta^{56}\text{Fe}$ values in the residual seawater $\text{Fe(II)}_{\text{aq}}$ (Fig. 2). The interbedded, pyrite-bearing shales generally have negative $\delta^{56}\text{Fe}$ values, so if such a scenario occurred, the shales cannot be the high- $\delta^{56}\text{Fe}$ reservoir that an equilibrium precipitation model requires.

There are three major Mo sinks in modern marine environments, sorption to Mn oxides, sequestration into suboxic sediments, and removal into sulfides under euxinic conditions, but only the first two produce significant Mo isotope fractionations (Brucker et al., 2009 and references therein). An additional, but minor, Mo sink is sequestration into biological material, a process that produces a significant Mo isotope fractionation (Zerkle et al., 2011). However, none of these processes is a likely explanation of the

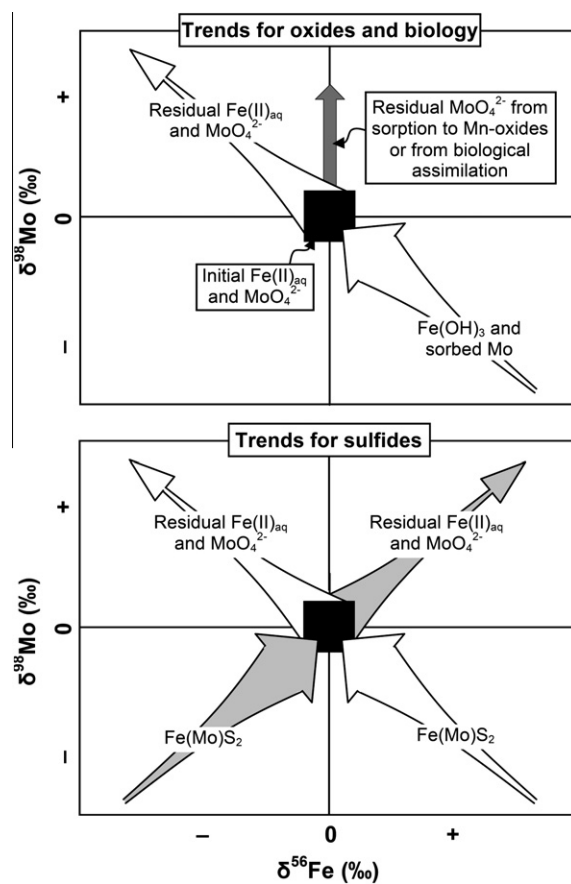


Fig. 2. Schematic illustration of Fe and Mo isotope variations for various pathways in marine environments as a function of Fe(III) oxide/hydroxide [Fe(OH)_3], Mn oxide, biological assimilation, and Fe sulfide precipitation. For simplicity, the assumed starting aqueous $\delta^{56}\text{Fe}$ and $\delta^{98}\text{Mo}$ values are both 0‰. *Upper panel:* The open arrows represent coupled Fe and Mo isotope fractionation that occurs during Fe oxide precipitation (abiological or biologically mediated) and subsequent sorption of MoO_4^{2-} based on published fractionation factors for Fe(OH)_3 precipitation ($\alpha_{\text{Fe(OH)}_3-\text{Fe(II)}_{\text{aq}}} > 1$; Croal et al., 2004; Wu et al., 2010) and Mo sorption to Fe(OH)_3 ($\alpha_{\text{Mo}_{\text{sorb}}-\text{MoO}_4^{2-}} < 1$; Goldberg et al., 2009). These fractionation factors produce Fe and Mo isotope compositions of residual $\text{Fe(II)}_{\text{aq}}$ and MoO_4^{2-} that must trend into the upper left quadrant, balanced by Fe(OH)_3 and sorbed Mo that lie in the lower right quadrant. The vertical gray arrow along the abscissa indicates the expected trend for Fe and Mo isotope evolution during Mo sorption to Mn oxides or biological assimilation of Mo. *Lower panel:* Similar to those in the upper panel, the open and gray pairs of arrows represent coupled Fe and Mo isotope fractionation based on published fractionation factors for FeS_2 precipitation from $\text{Fe(II)}_{\text{aq}}$ [open arrows: $\alpha_{\text{FeS}_2-\text{Fe(II)}_{\text{aq}}} > 1$ (Polyakov and Sultantov, 2011); gray arrows: $\alpha_{\text{FeS}_2-\text{Fe(II)}_{\text{aq}}} < 1$ (Guilbaud et al., 2011)] and Mo assimilation into sulfides ($\alpha_{\text{Mo}_{\text{sorb}}-\text{MoO}_4^{2-}}$; Neubert et al., 2008a). In both panels, the widths of the arrow shafts schematically represent how the relative sizes of the pools change during fractionation. The term “ Fe(Mo)S_2 ” represents Fe sulfides with sequestered Mo.

data presented here. Although sorption of Mo to Mn oxides is the dominant control on the Mo isotope composition of the modern, fully-oxygenated ocean (Kashiwabara et al.,

2009), and this process has a larger fractionation factor than sorption of Mo to Fe oxides (Goldberg et al., 2009), this mechanism can be discounted as a significant controller of the Mo isotope composition of the Neoproterozoic ocean for several reasons. At a given pH, Mn oxide precipitation begins at a higher Eh than Fe oxide precipitation, and so it is expected that in the Archean, which had a less oxidizing ocean than the modern Earth, Fe oxides were more important in determining the Mo isotope composition of seawater than Mn oxides. This idea is supported in general by the large volume of Fe deposited in the Transvaal Basin relative to Mn at this time (Beukes, 1987; Klein, 2005; Beukes and Gutzmer, 2008), and in particular by the much greater Fe content relative to Mn in the cores studied here (Schröder et al., 2006). Furthermore, below pH 8, abiotic Mn oxidation does not proceed without a catalyst (Murray and Brewer, 1977; Diem and Stumm, 1984), making Fe oxides a more likely controller of Mo isotope composition in marine settings in the absence of O₂-utilizing Mn oxidizing bacteria. Finally, a purely Mn oxide control of Mo isotope fractionation would decouple Mo and Fe isotope variations, producing a vertical array of data in $\delta^{56}\text{Fe}$ – $\delta^{98}\text{Mo}$ space away from that of the starting material (Fig. 2).

Similar to the fractionation observed for sorption of Mo to Fe-oxides, sequestration of Mo into suboxic, anoxic, or weak euxinic sediments is accompanied by a generally negative aqueous Mo–sediment Mo fractionation factor (Siebert et al., 2003, 2006; Poulson et al., 2006; Neubert et al., 2008a). However, as is the case for Mo sorption to Mn-oxides, or sulfides, sequestration of Mo into suboxic sediments would decouple Fe and Mo isotope variations. Moreover, such models do not explain the similar Mo and Fe isotope variations observed in the carbonates and interbedded shales.

Biological assimilation of Mo into enzymes by nitrogen-fixing microbes has also been shown to impart a negative fractionation resulting in an isotopically heavy residual pool of MoO₄²⁻ (Liermann et al., 2005; Wasylenki et al., 2007; Zerkle et al., 2011), but as is the case with Mo sorption to Mn oxides, or sequestration into suboxic sediments or sulfides, such a process would decouple Fe and Mo isotope variations (Fig. 2). Variable extents of Mo assimilation by microorganisms over time could, however, lead to temporal variability in the average $\delta^{98}\text{Mo}$ value of the MoO₄²⁻ pool of the Archean ocean.

Finally, we address alternative means of Fe(II) oxidation other than by reaction with free O₂. Anoxygenic photosynthetic Fe(II) oxidation (APIO) is known to produce low- $\delta^{56}\text{Fe}$ residual Fe(II)_{aq} (Croal et al., 2004), and has been shown to potentially produce large masses of Fe oxide (Konhauser et al., 2002; Kappler et al., 2005). Paleogeographic reconstructions of the Transvaal Basin, however, suggest that Fe deposition occurred only in the deep basin and not in shallow water environments (Beukes and Gutzmer, 2008). In contrast, Fe(II) oxidation coupled directly to photosynthesis would result in Fe oxide deposition in all water depths (i.e., in the shallow water photic zone as well as the deep basin). This consideration, together with the presumed requirement for some free atmospheric O₂ to introduce Mo to the ocean as soluble MoO₄²⁻, forms

the basis of our assumption that reaction of Fe(II) with O₂ produced by oxygenic photosynthesis – as opposed to anoxygenic photosynthetic Fe(II) oxidation – was responsible for Fe oxide deposition in the Transvaal Basin.

4.3. Dispersion/reaction model

4.3.1. Fe–Mo isotope fractionation

The dispersion/reaction model described in Section 2.4 was developed to help test the conceptual hypothesis that oxidation of aqueous Fe(II) by photosynthetically produced O₂ and subsequent sorption of aqueous Mo to Fe oxide/hydroxides in a hypothetical Archean basin could broadly account for the Fe and Mo isotope compositions of the carbonate samples studied here (Fig. 2). It was also designed to help constrain the amount of O₂ required to produce the isotopic fractionations observed, and to evaluate the interplay between O₂ and Fe(II) diffusion and oxidation. The results of three runs of the model are shown in Fig. 3. The solid profiles were produced using the initial conditions listed in Table 1. The other profiles were produced by either an increase in the lower bound of Fe(II)_{aq} to 1000 μM (an order of magnitude increase; long-dashed profiles) or by a decrease in the rate of O₂ release in the photic zone ($R_{\text{O}_2\text{-rel}}$) to 0.2% of the modern O₂ production rate (an order of magnitude decrease; short-dashed profiles). The sensitivity of the model to these and other parameters is discussed below. In the model, O₂ is produced in the photic zone and transported downward by eddy diffusion where it reacts with Fe(II)_{aq} that diffuses upward. The model predicts that the O₂ concentration will decrease from the photic zone downward, and the Fe(II)_{aq} concentration will decrease from the base of the profile upward to the point where Fe(II)_{aq} is essentially fully oxidized by O₂ (Fig. 3a and b). At the depth of this intersection, Fe(OH)₃ concentrations reach a maximum, and this region is termed the “reaction zone” (Fig. 3c; horizontal gray bands). It should be stressed that the depth of the reaction zone is not set by the model, but rather evolves to a steady-state condition based on the input parameters, principally the lower bound of Fe(II)_{aq} and the $R_{\text{O}_2\text{-rel}}$. Aqueous MoO₄²⁻ concentrations decrease with depth in the profile down to the reaction zone and are then essentially constant at lower depths (Fig. 3d). The profile of Mo_{sof} parallels that of Fe(OH)₃ (Fig. 3e). Note that in run 1, the reaction zone is ~250 m below the photic zone, indicating that downward transport of O₂ produced in the photic zone is sufficient to oxidize large amounts of upward-diffusing Fe(II)_{aq}. In runs 2 and 3, which represent extreme conditions, the top of the reaction zone overlaps the bottom of the photic zone by only ~3 m, but the bulk of the oxidation takes place below 100 m. Note that these spatial relationships are insensitive to the modeled depth of the photic zone (the depth over which O₂ is produced) because any change would result in a proportional change of the depth of each reaction zone.

Our model predicts that isotopic exchange in the reaction zone largely controls the Fe and Mo isotope fractionations produced by Fe(OH)₃ precipitation and Mo sorption, and it reproduces the positive $\delta^{98}\text{Mo}$ and negative $\delta^{56}\text{Fe}$

values recorded in the samples analyzed here. Although $\delta^{56}\text{Fe}$ values in the shallow part of the water column are extremely negative (between $\sim -10\text{‰}$ and -20‰ ; Fig. 3f), the dissolved Fe contents at shallow water depths in the reaction model are vanishingly small because oxidation is nearly complete (Fig. 3b), so such values minimally influence what may be sequestered into the sediments from seawater. Because the measured Fe and Mo isotope data represent average compositions of the water in the zone where they were incorporated into the sediments, it is necessary to compare the measured isotopic compositions of the carbonate and shale samples analyzed here to the weighted average $\delta^{56}\text{Fe}$ and $\delta^{98}\text{Mo}$ values for residual $\text{Fe(II)}_{\text{aq}}$ and MoO_4^{2-} from the reaction zone. In general, the modeling results demonstrate that a combination of O_2 -driven $\text{Fe(II)}_{\text{aq}}$ oxidation and MoO_4^{2-} sorption to Fe(OH)_3 can produce $\delta^{98}\text{Mo}_{\text{Mo-aq}}$ and $\delta^{56}\text{Fe}_{\text{Fe(II)aq}}$ values consistent with those observed in the carbonates and shales. Because of the scatter in the shale data, likely caused by variable mineral compositions and clastic contributions, we focus on the carbonate data for comparison to the model results (Fig. 4), but it is important to stress that the Fe and Mo isotope data from the shales is entirely consistent with those of the carbonates.

The calculated weighted average $\delta^{56}\text{Fe}$ and $\delta^{98}\text{Mo}$ values are sensitive to six parameters of the model (Fig. 4a–e): the two fractionation factors used ($\alpha_{\text{Fe(OH)}_3\text{-Fe(II)}_{\text{aq}}}$ and $\alpha_{\text{Mo}_{\text{sorb}}\text{-MoO}_4^{2-}}$), the portion of the reaction zone that is integrated, the depth of the basin modeled, the rate of O_2 release in the photic zone ($R_{\text{O}_2\text{-rel}}$), and the coefficient of MoO_4^{2-} sorption to Fe(OH)_3 . The model results are almost completely insensitive to the values chosen for the lower bound of $\text{Fe(II)}_{\text{aq}}$ and the upper bound of MoO_4^{2-} (Fig. 4f). Changing the $\alpha_{\text{Fe(OH)}_3\text{-Fe(II)}_{\text{aq}}}$ fractionation from 1.004 to 1.0032 (maximum and mean values, respectively, observed in Wu et al., 2010) led to a minor but distinct shift in weighted average $\delta^{56}\text{Fe}_{\text{Fe(II)aq}}$ values (Fig. 4a). Model runs that used a $\alpha_{\text{Mo}_{\text{sorb}}\text{-MoO}_4^{2-}}$ value of 0.997 produced weighted average $\delta^{98}\text{Mo}_{\text{Mo-aq}}$ values that fall within the range of the observed data, whereas using a $\alpha_{\text{Mo}_{\text{sorb}}\text{-MoO}_4^{2-}}$ fractionation of 0.999, equal to the experimental results of Goldberg et al. (2009), led to more modest increases in $\delta^{98}\text{Mo}_{\text{Mo-aq}}$ values, near the lower boundary of the observed data (Fig. 4a). Integration of the $\delta^{56}\text{Fe}$ and $\delta^{98}\text{Mo}$ values from either the top half or bottom half of the reaction zone produced weighted average $\delta^{56}\text{Fe}$ values of -3.7‰ or -1.0‰ , respectively, but the weighted average $\delta^{98}\text{Mo}$ values are virtually identical to those produced by integrating the entire reaction zone (Fig. 4b). Changing the depth of the basin by ± 250 m from our preferred value of 500 m changed the calculated average $\delta^{56}\text{Fe}$ and $\delta^{98}\text{Mo}$ values by a maximum of $\sim 30\%$ (Fig. 4c). The values of $R_{\text{O}_2\text{-rel}}$ tested had a significant influence on the average $\delta^{98}\text{Mo}$ value, but not the $\delta^{56}\text{Fe}$ value (Fig. 4d). The values of the MoO_4^{2-} sorption coefficient chosen also had a significant influence on only the average $\delta^{98}\text{Mo}$ values calculated (Fig. 4e). It is important to stress, however, that if the sorption coefficient is varied by an order of magnitude, the average $\delta^{98}\text{Mo}$ values remained roughly within the field of measured data.

A reasonable range of values produce results that plot within the field of data measured from Neoproterozoic carbonates, despite uncertainties in many parameters. The majority of the scatter in the measured $\delta^{56}\text{Fe}$ values (Fig. 4) can be well explained by variations in the portion of the reaction zone that is averaged (Fig. 4b), because it is unlikely that the depth of the reaction zone was static. Variable rates of O_2 production in the Neoproterozoic could potentially account for the large amount of scatter in the measured $\delta^{98}\text{Mo}$ values (Fig. 4e). Additionally, mixing of residual $\text{Fe(II)}_{\text{aq}}$ and MoO_4^{2-} in the reaction zone with $\text{Fe(II)}_{\text{aq}}$ and MoO_4^{2-} that have $\delta^{56}\text{Fe}$ and $\delta^{98}\text{Mo}$ values equal to the initial compositions could produce intermediate $\delta^{56}\text{Fe}$ and $\delta^{98}\text{Mo}$ values. Such mixing could occur by fluctuations in the depth at which the reaction zone intersected the seafloor (e.g., Kendall et al., 2010). Finally, we note that there is also uncertainty in the chosen initial $\delta^{56}\text{Fe}$ and $\delta^{98}\text{Mo}$ values because, as noted above, the fractionation factor between $\text{Fe(II)}_{\text{aq}}$ and low Fe carbonates is unknown, and temporation variations in biological Mo assimilation could alter the residual pool of MoO_4^{2-} (Section 4.2).

4.3.2. Archean ocean oxygenation

The dispersion/reaction model allows us to put constraints on the concentration of O_2 in the photic zone of the basin in which the carbonates and shales were deposited. Based on the preferred values of the model parameters listed in Table 1, the calculated average dissolved O_2 concentration for the water column sampled by these carbonates was ~ 35 M (Fig. 5), a value that is $\sim 12\%$ of the modern near-shore photic zone O_2 concentration of ~ 300 μM . The most sensitive parameters that affect O_2 concentrations are the lower bound of the $\text{Fe(II)}_{\text{aq}}$ concentration and the rate of O_2 release in the photic zone ($R_{\text{O}_2\text{-rel}}$) (Fig. 5). An increase in the initial $\text{Fe(II)}_{\text{aq}}$ concentration would result in a greater amount of Fe(OH)_3 production and a concomitant drawdown of O_2 in the photic zone, but even an $\text{Fe(II)}_{\text{aq}}$ value of 1000 μM , a rather high estimate for the Archean ocean (Ewers, 1980; Morris and Horwitz, 1983; Holland, 1984), will result in an average photic zone O_2 concentration of ~ 14 μM , assuming an $R_{\text{O}_2\text{-rel}}$ of 2% that of the modern rate of production (Figs. 3 and 5). An increase or decrease in the $R_{\text{O}_2\text{-rel}}$ produces a roughly proportional increase or decrease in the resulting average O_2 concentration (Fig. 5), but an $R_{\text{O}_2\text{-rel}}$ value of 2% is the minimum necessary to reproduce the measured extent of Mo isotope fractionation, assuming the preferred values for all other parameters (Fig. 4). The only other parameter that has an effect on the average photic zone O_2 concentration is the depth of the basin, although over a range of depths from 250 to 750 m, the calculated O_2 concentration ranged from 20 to 47 μM (Fig. 5). Finally, it should be stressed that the model assumed an upper boundary condition for O_2 that was in equilibrium with an atmospheric $p\text{O}_2$ of 10^{-5} PAL (2.52×10^{-9} μM ; Table 1) and thus does not directly address the question of atmospheric O_2 concentrations. In fact, varying this value over 13 orders of magnitude (from 2.52×10^{-6} to 2.52×10^{-19} μM , or the values assuming equilibrium with a atmospheric $p\text{O}_2$ of 10^{-2} to 10^{-15} PAL) had essentially no effect on the

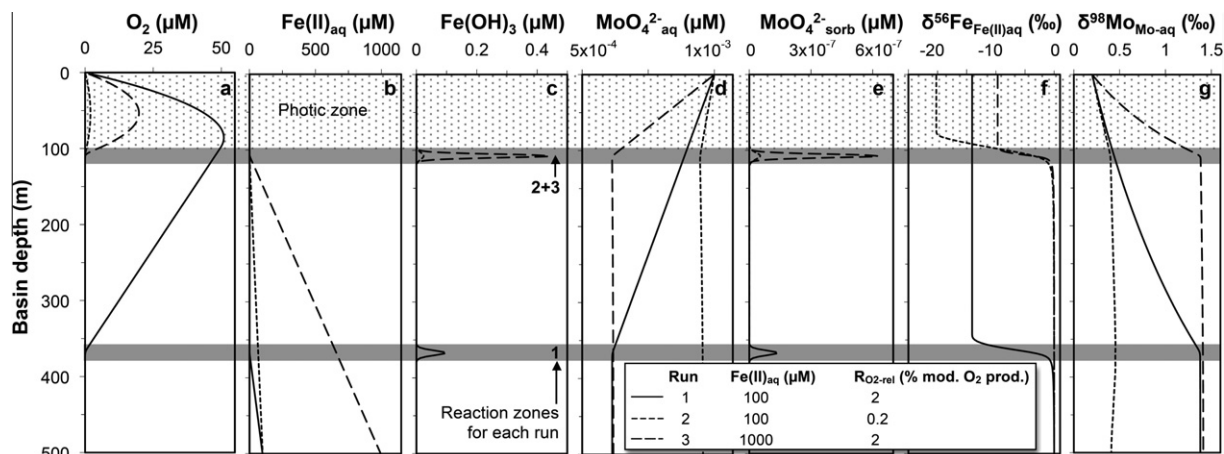


Fig. 3. Representative results of the dispersion/reaction model. Concentrations and isotopic gradients in the upper water column are shown, relative to steady-state conditions, for O₂ (a), Fe(II)_{aq} (b), Fe(OH)₃ (c), MoO₄²⁻_{aq} (d), and MoO₄²⁻_{sorb} (e), as well as Fe(II)_{aq} and MoO₄²⁻_{aq} isotope compositions (f and g). Calculation of the one-dimensional dispersion/reaction model is described in Section 2.4. Each panel shows the model results produced by use of the preferred values for each parameter in Table 1 (solid lines), by decreasing the rate of O₂ release in the photic zone (R_{O₂-rel}) (dotted lines), or by increasing the lower boundary condition for Fe(II)_{aq} (long dashed lines). The stippled area spanning 0–100 m indicates the depth of the photic zone. The gray shaded areas below the photic zone indicate the reaction zones for various model runs, numbered 1 through 3, which are defined where Fe(OH)₃ precipitation occurs.

calculated average O₂ concentration of the photic zone (Fig. 5).

Although R_{O₂-rel} in the Archean ocean is not known, a rate roughly equivalent to the mean value for modern oceans produced aqueous Mo fractionations comparable to the observed data (Fig. 4). Given evidence that the concentration of nutrients in the Neoproterozoic ocean, most importantly orthophosphate (PO₄²⁻), was likely the same as today (Planavsky et al., 2010a), it is reasonable to assume that the overall rates of organic carbon and O₂ production in the Neoproterozoic were the same as those of the modern ocean. An R_{O₂-rel} value of 2% is greater than that estimated for the modern ocean (<1%, based on rates of net primary production and organic matter burial; Schlesinger, 1997), but the modern value is based in part on near complete oxidation of organic matter that settles in the modern deep ocean, a process that would have been less efficient in the Archean because of the existence of an anoxic deep ocean. Additionally, less efficient aerobic oxidation of photosynthetically-produced organic matter, over the water column as a whole, would lead to a greater fraction of net O₂ release. Due to variations in the supply of nutrients and organic matter recycling, however, the value of R_{O₂-rel} would have varied with time, on both seasonal and longer time scales.

The range of water column O₂ concentrations indicated by the modeling (a few to a few tens of μM; see Fig. 5) is consistent with previous estimates. Kasting (1992) calculated an Archean ocean O₂ concentration of ~20 μM using a three-box model, although the model excluded any O₂ sinks. Kendall et al. (2010) analyzed shales from the same cores as the carbonates studied here and estimated O₂ contents of ~10–100 μM for the Transvaal Basin, although those authors acknowledge that this is based on comparison of their geochemical data with those

from modern settings and that such a comparison is not calibrated. Our range is somewhat inconsistent with the range of 0.05–5 μM estimated by Planavsky et al. (2010b) based on REE data that suggest the Eh of the Archean ocean was such that Fe could be oxidized, but not cerium or manganese. These estimates, including those proposed here, are only potentially valid as gross averages over millions to tens of millions of years. The O₂ concentration of the photic zone in the Neoproterozoic likely varied tremendously over shorter time scales because of variable rates of O₂ production, variable inputs of Fe(II)_{aq}, and the large quantity of other reduced sinks in the surface environment (e.g., volcanic gases and igneous and metamorphic rocks).

Overall, the data and models presented here are consistent with a water column above a Neoproterozoic carbonate platform margin that had a deep Fe(II)-rich layer that was overlain by a relatively O₂-rich layer (Fig. 6). Quantitative oxidation of Fe(II) at the oxic–anoxic boundary produced Fe(OH)₃ particles that had Fe isotope compositions nearly identical to the bottom water Fe(II)_{aq}, which left behind very small quantities of isotopically light Fe(II)_{aq}. Sorption of MoO₄²⁻ to Fe(OH)₃ led to generation of isotopically heavy residual aqueous MoO₄²⁻, and to deposition of isotopically light sorbed MoO₄²⁻. The isotopically light residual Fe(II)_{aq} and heavy MoO₄²⁻ pools were incorporated into carbonate on the platform slope, thus recording the seawater Fe and Mo isotope compositions. The model predicts that Fe-rich deposits would have accumulated in the deepest parts of the basin below where the carbonates and shales studied here were deposited, and will have near-zero to slightly positive δ⁵⁶Fe values and near-zero δ⁹⁸Mo values. Future analysis of the Fe and Mo isotope compositions of iron formations will provide a test of this model.

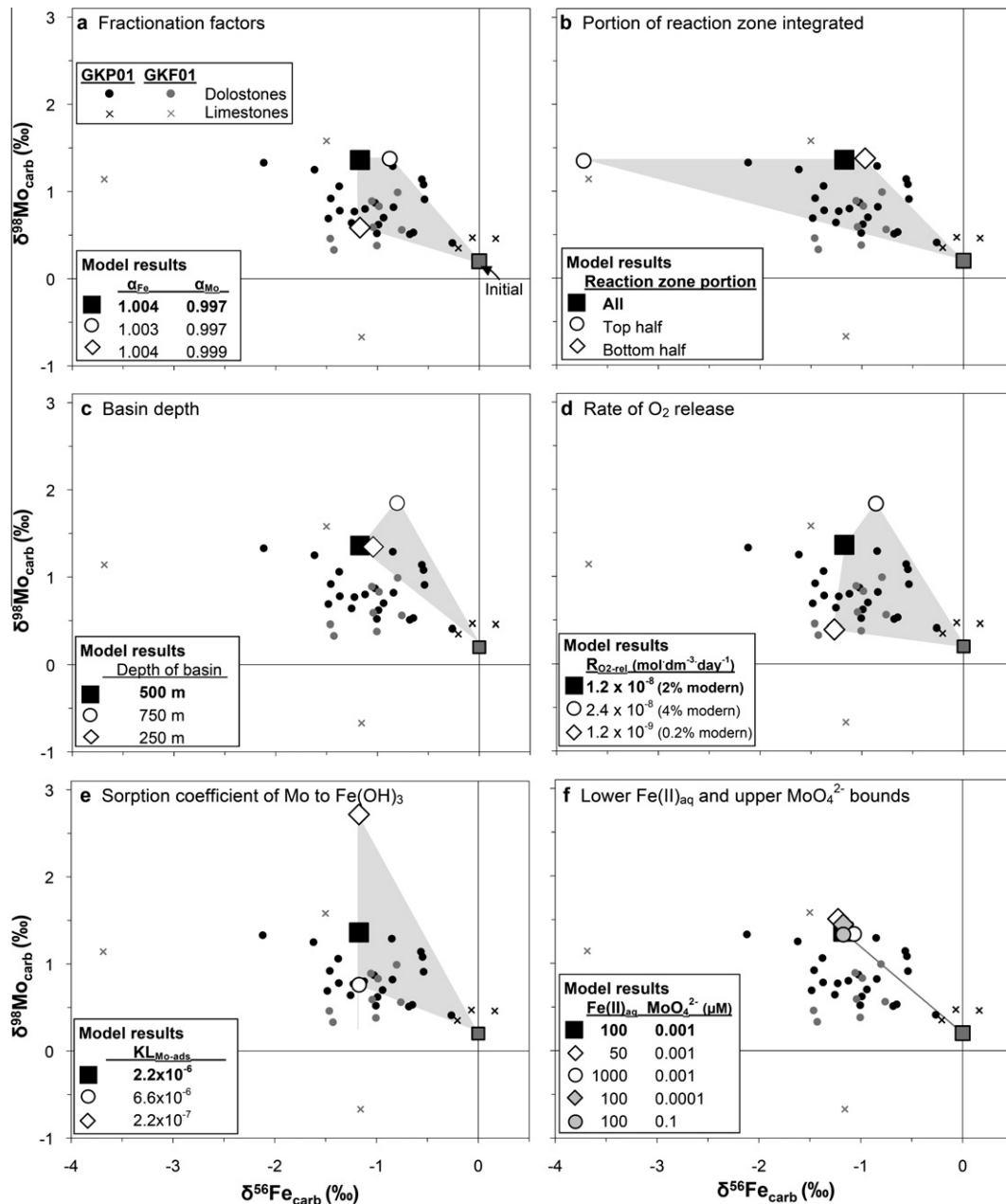


Fig. 4. Weighted average $\delta^{56}Fe$ and $\delta^{98}Mo$ values from the reaction zones of various model runs and the measured $\delta^{56}Fe$ and $\delta^{98}Mo$ values of carbonates studied here (see Fig 1 and Table EA-2-2). For the carbonate data, circles represent dolostones and crosses represent limestones from cores GKP01 (black symbols) and GKF01 (gray symbols). Each panel illustrates the sensitivity of the model to a key parameter, namely the fractionation factors associated with $Fe(OH)_3$ precipitation from $Fe(II)_{aq}$ and MoO_4^{2-} sorption to $Fe(OH)_3$ (a), the portion of the reaction zone that is integrated (b), the depth of the basin (c), the rate of O_2 release in the photic zone (d), the coefficient of MoO_4^{2-} sorption to $Fe(OH)_3$ (e), and the lower $Fe(II)_{aq}$ and upper MoO_4^{2-} bounds (f). The gray square in each panel represents the initial $\delta^{56}Fe$ value of $Fe(II)_{aq}$ and $\delta^{98}Mo$ value of MoO_4^{2-} of the modeled Archean ocean ($\delta^{56}Fe = 0\text{‰}$, and $\delta^{98}Mo = 0.2\text{‰}$). The black square in each panel represents the model results produced by the parameter values listed in Table 1. Circles and diamonds represent model results produced by varying the parameter noted in each panel. The gray areas are used to encompass the potential $\delta^{56}Fe$ – $\delta^{98}Mo$ space that could be occupied by varying each parameter and mixing with $Fe(II)_{aq}$ and MoO_4^{2-} that have the initial Fe and Mo isotope compositions.

4.4. Paleoenvironmental conditions in the Neoproterozoic

The isotopic data reported here are part of a larger suite of geochemical data from the Agouron drill cores recovered

from the Campbellrand–Malmani carbonate platform of South Africa (Fig. 7). Collectively, these data provide a thorough understanding of the platform depositional system and support the interpretation that photosynthesis

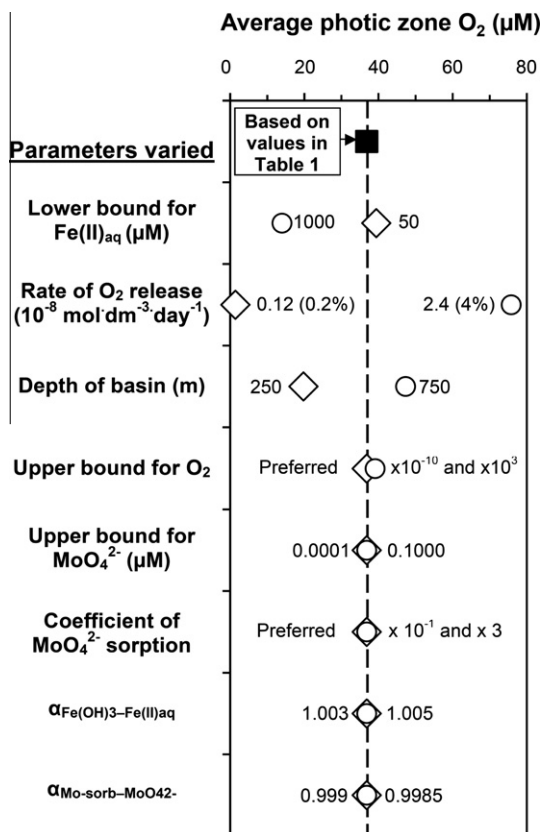


Fig. 5. Sensitivity of calculated photic zone O_2 concentrations to variations in key model parameters. The O_2 concentrations are averages produced by integrating each 2 m depth interval from the top 100 m of the modeled basin for each run (cf. Fig. 3). The black square at the top and the vertical dashed line represent the average O_2 concentration produced using the preferred value of each parameter (see Table 1). The other symbols represent low (open diamonds) and high (open circles) values of each parameter.

produced sufficient O_2 in the photic zone to oxidize Fe-rich bottom waters under conditions of low atmospheric O_2 . The generally near-zero $\delta^{13}C$ values for the majority of carbonates above the shallow-water Vryburg Formation indicate that the carbonates may be confidently taken to reflect precipitation from seawater (Fig. 7; Fischer et al., 2009). The only significantly negative excursions in $\delta^{13}C$ values in this section are from shale-rich samples or those that are Fe-rich. $\delta^{18}O$ values approach those expected for precipitation from ocean water that had a near-zero $\delta^{18}O$ value, assuming precipitation between 20 and 50 °C (Kim and O'Neil, 1997). The offset between the calcite-dominated carbonates of the Vryburg, Boomplaas, Lokammona, and lower Monteville formations (lowermost units of the core, Fig. 7) and the dolostones of the upper Monteville, Nauga, and Klein Naute formations is equivalent to the expected fractionation factor between dolomite and calcite ($\sim 5\%$; Chacko and Deines, 2008). The slightly lower $\delta^{18}O$ values than those expected for precipitation from seawater may reflect a slightly negative $\delta^{18}O$ value for seawater or moderate post-formation re-equilibration. It is important to stress, however, that $\delta^{18}O$ and $\delta^{13}C$ values only covary in the

shale-rich samples, indicating that the majority of carbonates are not significantly diagenetically altered, as discussed in Fischer et al. (2009). Sulfur isotope variations support the interpretation that photosynthetic O_2 production in the Late Archean ocean had not yet produced high levels of atmospheric O_2 . The moderately positive to moderately negative $\delta^{34}S$ values suggest bacterial sulfate reduction under limited sulfate conditions (e.g., Canfield, 2001), where most of the $\delta^{34}S$ values are equal to or lower than that estimated for seawater sulfate at 2.6 Ga ($\delta^{34}S \approx 9\%$; Canfield and Farquhar, 2009). This is consistent with the moderate O_2 levels inferred for the photic zone. Importantly, mass-independent sulfur fractionations ($\Delta^{33}S \neq 0$) measured from the same sulfide samples (Fig. 7; Ono et al., 2009b; Kendall et al., 2010) suggest that the atmospheric O_2 concentration could not have been greater than 10^{-5} PAL at this time (Pavlov and Kasting, 2002). We therefore conclude that photosynthetic O_2 production in the photic zone had not yet provided significant free O_2 to the atmosphere, although some limited subaerial oxidation of sedimentary sulfides may have been responsible for producing some of the seawater sulfate (e.g., Ono et al., 2009b; Kendall et al., 2010), as well as mobilizing Mo as MoO_4^{2-} .

The similar geologic units and sequences of the Pilbara Craton of Australia and the Kaapvaal Craton of South Africa invite comparison of geochemical data, and a composite section from both cratons is shown in Fig. 8, based on the time-stratigraphic model for the Hamersley Province determined by Czaja et al. (2010). Previously reported U–Pb ages of key marker beds and unit boundaries from the succession of Ghaap Group units studied here [summarized by Knoll and Beukes (2009)] were used to interpolate ages for each sample, assuming uniform depositional rates between each reported age. Although these depositional rates are gross averages, reasonable changes in these rates would not change the overall trends in chemical and isotopic compositions.

The temporal evolution of Fe isotope compositions of carbonates and shales measured here very closely matches that of carbonates of the Hamersley Province of Western Australia (Fig. 8). Such a correlation is consistent with the hypothesis that the Kaapvaal and Pilbara cratons were once part of a single continental block, or at a minimum, that they record similar geochemical cycling in similar marine environments (e.g., Beukes and Gutzmer, 2008). The oldest measured instances of light $\delta^{56}Fe$ values from the South African carbonates are from samples from the Monteville Formation, the deposition of which started at roughly the same time as formation of the Marra Mamba Iron Formation, in the Hamersley Province. Czaja et al. (2010) showed that the Marra Mamba IF has near-zero $\delta^{56}Fe$ values, and this is expected for accumulation of Fe oxides based on the dispersion/reaction model presented here. This in turn would produce negative $\delta^{56}Fe$ values for low-Fe, Ca–Mg carbonates, and low-Fe shales, as observed in the current study, following our interpretation that these rocks represent the residual, seawater $Fe(II)_{aq}$ pool, which mass-balance indicates is a much smaller Fe pool than that contained in the iron formations. At about the time Marra Mamba IF deposition ceased in the

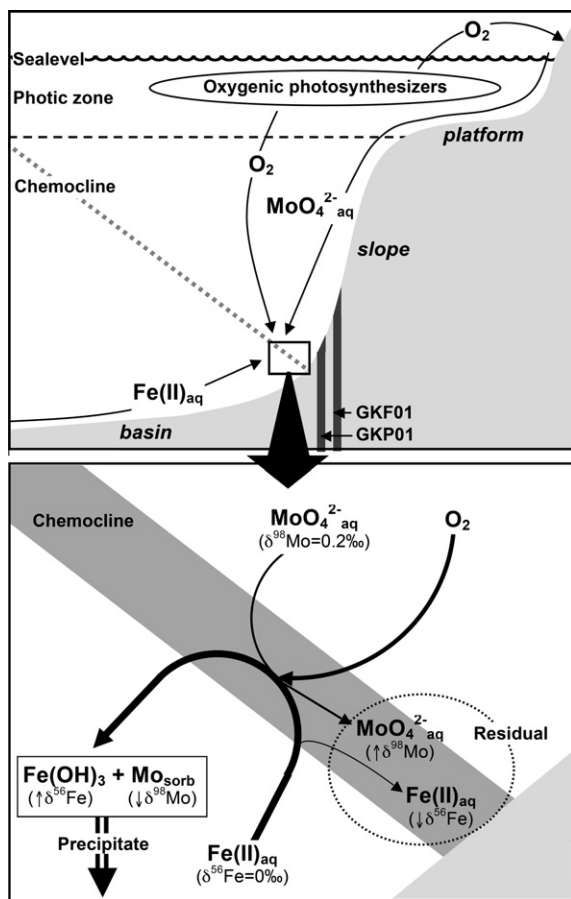


Fig. 6. Illustration of Fe and Mo pathways and isotope variation in the Neoproterozoic Transvaal Basin. Oxygenic photosynthesizers in the photic zone produced O_2 , some of which escaped to the atmosphere and mobilized crustal Mo to produce soluble molybdate (MoO_4^{2-} aq). Oxygen also diffused down into deeper waters, below the photic zone to the chemocline. Details of the reactions taking place at the chemocline are shown in the lower panel. Reaction of free O_2 with hydrothermally sourced aqueous ferrous Fe [$Fe(II)_{aq}$] produced insoluble isotopically heavy Fe(III) oxide/hydroxides [$Fe(OH)_3$] to which isotopically light MoO_4^{2-} aq sorbed, both of which were sequestered in oxide deposits that accumulated in deeper sections of the basin relative to the GKF01 and GKP01 cores. The isotopically light residual $Fe(II)_{aq}$ and heavy MoO_4^{2-} aq were incorporated into carbonates and shales deposited on the slope, recording the Fe and Mo isotope compositions of the Neoproterozoic ocean water. Changes in $Fe(II)_{aq}$ flux would move the position of the chemocline (reaction zone) up or down. Note the depth axis is not to scale.

Hammersley Province, the $\delta^{56}Fe$ and $\delta^{98}Mo$ values of carbonates from South Africa show a gradual increase and decrease, respectively (Fig. 8a and b). We interpret this to be a direct response to the cessation of extensive iron formation deposition, reflecting movement in the $\delta^{56}Fe$ and $\delta^{98}Mo$ values in the shallow ocean toward those of the deep ocean and continental input, respectively. The subsequent decrease in $\delta^{56}Fe$ and increase in $\delta^{98}Mo$ values in Fe-poor carbonates at ~ 2525 Ma correlates with the transition to a return of iron formation deposition (Kuruman IF in South

Africa; Brockman IF in Australia), which is also consistent with the dispersion/reaction model presented here. Although both the Kuruman and Brockman iron formations have a wide range in $\delta^{56}Fe$ values for specific bands or minerals, their average $\delta^{56}Fe$ value is zero (Johnson et al., 2003, 2008a; Heimann et al., 2010; Craddock and Dauphas, 2011), as expected from the dispersion/reaction model.

The top of the section illustrated in Fig. 8 corresponds with the Mt. McRae Shale (Australia). Previously measured Mo isotope compositions and concentrations, as well as other elemental abundances, of the Mt. McRae Shale have also been interpreted to indicate an increase in atmospheric O_2 at 2501 ± 8 Ma (Anbar et al., 2007; Duan et al., 2010; and Fig. 8b of this study), referred to as a “whiff” of O_2 , although no quantitative estimate was made regarding O_2 contents. The maximum $\delta^{98}Mo$ value reported from the Mt. McRae Shale ($\delta^{98}Mo = 1.86\%$; Duan et al., 2010) is only slightly higher than the maximum reported from the shales and carbonates analyzed here ($\delta^{98}Mo = 1.72\%$; Wille et al., 2007). The similar maximum $\delta^{98}Mo$ values might indicate that the amount of O_2 interpreted to have existed at 2.5 Ga was comparable to that needed to produce the Fe and Mo fractionations reported here at 2.68–2.50 Ga. We suggest, however, that such an estimate is not as well constrained as the coupled Fe–Mo isotope model described here. We conclude that covariation in Fe and Mo isotopes from 2.68 to 2.5 Ga provides strong evidence for variable oxygenation beyond a “whiff” at 2.5 Ga of at least the shallow ocean basin in which the sediments studied here were deposited.

5. SUMMARY AND CONCLUSIONS

Coupled Fe and Mo isotope analyses of carbonates and shales provide a new means of evaluating the oxygenation history of the Earth. The production of coupled Fe–Mo isotope variations in the shallow oceans requires formation of Fe oxides, consistent with the consensus that the marine Fe cycle in the Neoproterozoic and Paleoproterozoic was dominated by iron formation deposition. Molecular O_2 was required both to precipitate Fe well below the photic zone, as well as to mobilize crustal Mo. Our model of coupled Fe and Mo isotope fractionation requires both of these processes, and thus helps constrain the amount of O_2 needed to produce the measured isotopic compositions. We propose that iron oxides provide a unique coupling of the Fe and Mo isotope systems on the early Earth before the oceans were deeply oxidized, allowing transport of aqueous Fe to the shallow oceans. The modeling presented here indicates that a few to a few tens of μM of free O_2 (or a few percent of the present surface ocean O_2 concentration) could have been present in the photic zone, an amount required to produce the measured Fe and Mo isotope compositions. Thus, significant O_2 was present during deposition of Fe oxides in the deep Hammersley and Transvaal basins between 2.68 and 2.5 Ga. Although anoxygenic photosynthetic Fe(II) oxidation has been proposed as a mechanism for iron oxide formation (e.g., Kappler et al., 2005), this seems unlikely for

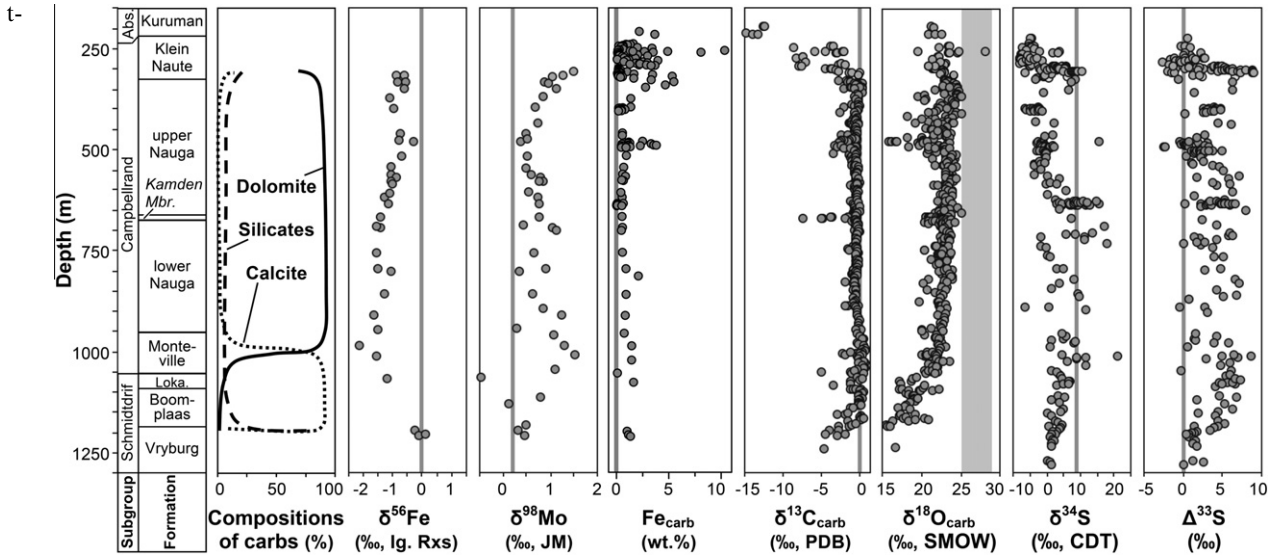


Fig. 7. A comparison of multiple sets of isotope and elemental data from Agouron drill cores GKP01 and GKF01, with the GKF01 data projected onto GKP01 based on inter-core stratigraphic correlations (Schröder et al., 2006; Knoll and Beukes, 2009; cf. Fig. 1). The plot of carbonate compositions, and the $\delta^{56}\text{Fe}$ and $\delta^{98}\text{Mo}$ data are the same as those in Fig. 1. Fe contents are from carbonates (this study and Kendall et al., 2010), $\delta^{13}\text{C}$ and $\delta^{18}\text{O}$ data are from carbonates (Fischer et al., 2009), and $\delta^{34}\text{S}$ and $\Delta^{33}\text{S}$ data are from sulfides (Ono et al., 2009b; Kendall et al., 2010). Abbreviations are the same as those in Fig. 1.

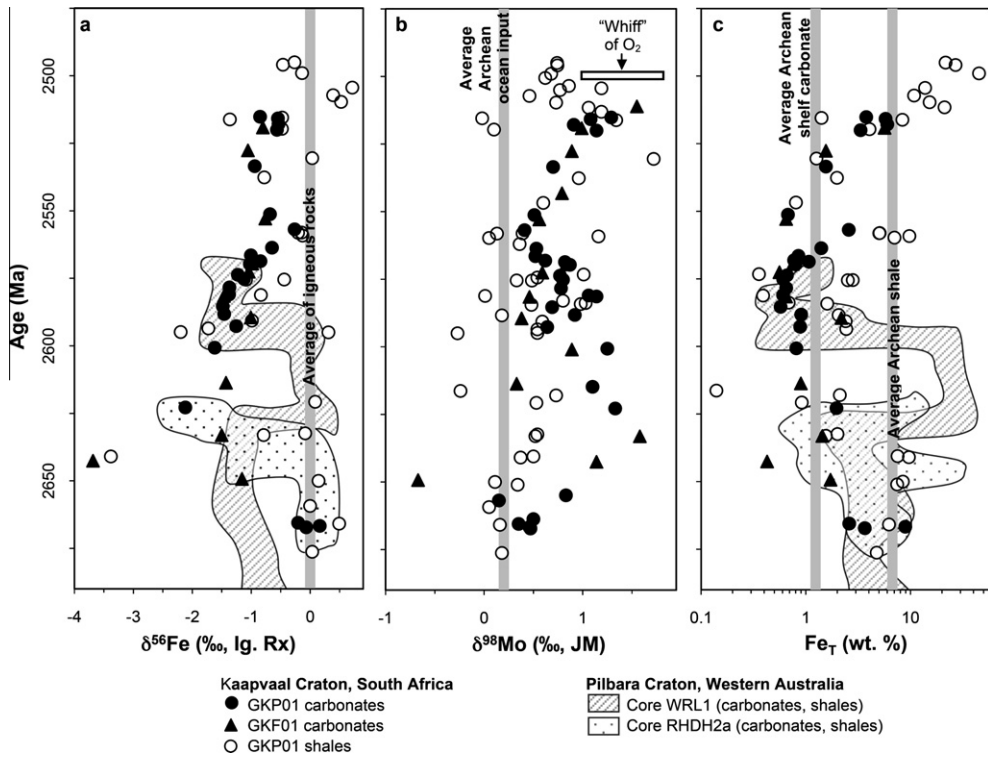


Fig. 8. Comparison of isotopic and geochemical data from the Pilbara (Australia) and Kaapvaal (South Africa) cratons. $\delta^{56}\text{Fe}$ values (a), $\delta^{98}\text{Mo}$ values (b), and total Fe (Fe_T) contents (c) for carbonates (black circles and triangles) and shales (open circles) plotted versus age of sample (see text for details of the age calculation). Circles represent samples from core GKP01 and triangles represent those from core GKF01. $\delta^{98}\text{Mo}$ values from carbonates were reported by Voegelin et al. (2010), and those from shales were reported by Wille et al. (2007). The hatched fields represent data from core WRL1 from the depocenter of the Hamersley Province in the Pilbara Craton, Western Australia, and the stippled fields represent data from core RHDH2a from the Ripon Hills area of the Hamersley Province (Czaja et al., 2010). The white box in panel (b) shows the range of $\delta^{98}\text{Mo}$ values from samples of the Mt. McRae Shale from Western Australia (Duan et al., 2010), the highest values representing a “whiff” of O_2 at 2501 Ma (Anbar et al., 2007). The vertical gray reference lines are the same as those in Fig. 1.

he time period covered here. In addition, these results, and the requirement of mobilized Mo, are consistent with the idea that prior to the GOE, consumption of O₂ by reduced volcanic gases and continental weathering would have buffered the O₂ flux to the atmosphere.

The results presented here only address the O₂ concentration of the photic zone, and not atmospheric O₂ concentrations, which may have remained less than 10⁻⁵ PAL, as constrained by mass-independent fractionation of sulfur (MIF-S). It is also important to note that the photic zone O₂ concentrations calculated here apply only to the section of basin represented by the cores studied, and may not reflect the Archean ocean as a whole. Because the build up of O₂ indicated by the model is directly dependent on O₂ release by photosynthesis, and because the model assumes an atmospheric O₂ concentration of 10⁻⁵ PAL, any portion of the ocean that did not have O₂ production (e.g., regions far from nutrient sources) would likely have been essentially devoid of free O₂.

The Neoproterozoic Transvaal Basin depositional system was, of course, more complex than what could be simulated with a one-dimensional dispersion/reaction model, but the model captures important aspects of the system and can largely explain the isotopic variations measured, as well as help constrain the O₂ concentration of the photic zone. Future work that could help test the ideas put forth here include experimental work to determine the fractionation factors of Mo isotopes upon sorption to Fe and Mn oxides under a variety of conditions (in particular, those of Archean seawater, including dissolved Si), and experiments to better understand Mo and Fe fractionation during carbonate precipitation. Additionally, coupled Fe and Mo isotope analyses of Fe oxides that were deposited contemporaneously with the carbonates and shales studied here, but more distal in the basin, should provide the mass balance for the light δ⁵⁶Fe and heavy δ⁹⁸Mo values here measured. The large mass of Fe and Mo in these oxides would, however, necessitate that their isotopic compositions would be only slightly fractionated from the initial compositions.

This study provides further evidence to the growing body of work that shows the evolution of atmospheric and marine O₂ was more complex than simply punctuated secular increases. This work also provides strong support for development of oxygenic photosynthesis by at least 2.7 Ga, because anoxygenic photosynthesis will not produce the coupled variations in the measured Fe and Mo isotope compositions. Additional studies of combined Fe and Mo isotopes of carbonates and shales may indicate how widespread ocean oxygenation was in the Archean and perhaps help to better constrain the absolute concentration of atmospheric O₂ and primary productivity.

ACKNOWLEDGEMENTS

Iron isotope analyses in Madison, WI were funded by the NASA Astrobiology Institute. Molybdenum isotope work in Bern was funded by Swiss National Science Foundation Grant 20021-

126759 to T.F.N. We thank H. Xu, H. Konishi, and J. Huberty for assistance with XRD analyses. We also thank D. Vance and C. Pearce, as well as two anonymous reviewers for comments on the manuscript. The manuscript also benefitted from discussions with P. Pufahl.

APPENDIX A. SUPPLEMENTARY DATA

Supplementary data associated with this article can be found, in the online version, at <http://dx.doi.org/10.1016/j.gca.2012.03.007>.

REFERENCES

- Albarède F. and Beard B. L. (2004) Analytical methods for non-traditional isotopes. In *Geochemistry of Non-Traditional Stable Isotopes* (eds. C. M. Johnson, B. L. Beard and F. Albarède). Mineralogical Society of America and Geochemical Society, Washington, DC, pp. 113–152.
- Anbar A. D., Duan Y., Lyons T. W., Arnold G. L., Kendall B., Creaser R. A., Kaufman A. J., Gordon G. W., Scott C., Garvin J. and Buick R. (2007) A whiff of oxygen before the Great Oxidation Event? *Science* **317**, 1903–1906.
- Anbar A. D. and Rouxel O. (2007) Metal stable isotopes in paleoceanography. *Annu. Rev. Earth Planet. Sci.* **35**, 717–746.
- Archer C. and Vance D. (2008) The isotopic signature of the global riverine molybdenum flux and anoxia in the ancient oceans. *Nat. Geosci.* **1**, 597–600.
- Barling J. and Anbar A. D. (2004) Molybdenum isotope fractionation during adsorption by manganese oxides. *Earth Planet. Sci. Lett.* **217**, 315–329.
- Barling J., Arnold G. L. and Anbar A. D. (2001) Natural mass-dependent variations in the isotopic composition of molybdenum. *Earth Planet. Sci. Lett.* **193**, 447–457.
- Beard B. L., Johnson C. M., Skulan J. L., Neelson K. H., Cox L. and Sun H. (2003a) Application of Fe isotopes to tracing the geochemical and biological cycling of Fe. *Chem. Geol.* **195**, 87–117.
- Beard B. L., Johnson C. M., Von Damm K. L. and Poulson R. L. (2003b) Iron isotope constraints on Fe cycling and mass balance in oxygenated Earth oceans. *Geology* **31**, 629–632.
- Beukes N. J. (1987) Facies relations, depositional environments and diagenesis in a major Early Proterozoic stromatolitic carbonate platform to basinal sequence, Campbellrand Subgroup, Transvaal Supergroup, southern Africa. *Sed. Geol.* **54**, 1–46.
- Beukes N. J. and Gutzmer J. (2008) Origin and paleoenvironmental significance of major iron formations at the Archean-Paleoproterozoic boundary. *Rev. Econ. Geol.* **15**, 5–47.
- Boudreau B. P. (1997) *Diagenetic Models and Their Implementation*. Springer, Berlin.
- Brocks J. J., Logan G. A., Buick R. and Summons R. E. (1999) Archean molecular fossils and the early rise of eukaryotes. *Science* **285**, 1033–1036.
- Brown P. N., Byrne G. D. and Hindmarsh A. C. (1989) VODE: a variable-coefficient ODE solver. *SIAM J. Sci. Stat. Comput.* **10**, 1038–1051.
- Brucker R. L. P., McManus J., Severmann S. and Berelson W. M. (2009) Molybdenum behavior during early diagenesis: insights from Mo isotopes. *Geochem. Geophys. Geosyst.* **10**, Q06010.
- Canfield D. E. (2001) Biogeochemistry of sulfur isotopes. In *Stable Isotope Geochemistry. Reviews in Mineralogy & Geochemistry* (eds. J. W. Valley and D. R. Cole). Mineralogical Society of America, Washington, D.C, pp. 607–636.

- Canfield D. E. (2005) The early history of atmospheric oxygen: homage to Robert Garrels. *Annu. Rev. Earth Planet. Sci.* **33**, 1–36.
- Canfield D. E. and Farquhar J. (2009) Animal evolution, bioturbation, and the sulfate concentration of the oceans. *Proc. Natl. Acad. Sci. USA* **106**, 8123–8127.
- Chacko T. and Deines P. (2008) Theoretical calculation of oxygen isotope fractionation factors in carbonate systems. *Geochim. Cosmochim. Acta* **72**, 3642–3660.
- Cloud, Jr., P. E. (1968) Atmospheric and hydrospheric evolution on the primitive earth. *Science* **160**, 729–736.
- Collier R. W. (1985) Molybdenum in the northeast Pacific Ocean. *Limnol. Oceanogr.* **30**, 1351–1354.
- Craddock P. R. and Dauphas N. (2011) Iron and carbon isotope evidence for microbial iron respiration throughout the Archean. *Earth Planet. Sci. Lett.* **303**, 121–132.
- Criss R. E. (1999) *Principles of Stable Isotope Distribution*. Oxford University Press, Oxford.
- Croal L. R., Johnson C. M., Beard B. L. and Newman D. K. (2004) Iron isotope fractionation by Fe(II)-oxidizing photoautotrophic bacteria. *Geochim. Cosmochim. Acta* **68**, 1227–1242.
- Czaja A. D., Johnson C. M., Beard B. L., Eigenbrode J. L., Freeman K. H. and Yamaguchi K. E. (2010) Iron and carbon isotope evidence for ecosystem and environmental diversity in the ~2.7 to 2.5 Ga Hamersley Province, Western Australia. *Earth Planet. Sci. Lett.* **292**, 170–180.
- Diem D. and Stumm W. (1984) Is dissolved Mn^{+2} being oxidized by O_2 in absence of Mn-bacteria or surface catalysts? *Geochim. Cosmochim. Acta* **48**, 1571–1573.
- Duan Y., Anbar A. D., Arnold G. L., Lyons T. W., Gordon G. W. and Kendall B. (2010) Molybdenum isotope evidence for mild environmental oxygenation before the Great Oxidation Event. *Geochim. Cosmochim. Acta* **74**, 6655–6668.
- Eigenbrode J. L. and Freeman K. H. (2006) Late Archean rise of aerobic microbial ecosystems. *Proc. Natl. Acad. Sci. USA* **103**, 15759–15764.
- Eigenbrode J. L., Freeman K. H. and Summons R. E. (2008) Methylhopane biomarker hydrocarbons in Hamersley Province sediments provide evidence for Neoproterozoic aerobicity. *Earth Planet. Sci. Lett.* **273**, 323–331.
- Erickson B. E. and Helz G. R. (2000) Molybdenum (VI) speciation in sulfidic water: stability and lability of thiomolybdates. *Geochim. Cosmochim. Acta* **64**, 1149–1158.
- Ewers W. E. (1980) Chemical conditions for the precipitation of banded iron-formations. In *Biogeochemistry of Ancient and Modern Environments* (eds. P. A. Trudinger, M. R. Walter and B. J. Ralph). Springer-Verlag, Berlin, pp. 83–92.
- Farquhar J., Bao H. and Thiemens M. (2000) Atmospheric influence of Earth's earliest sulfur cycle. *Science* **289**, 756–758.
- Farquhar J., Zerkle A. L. and Bekker A. (2011) Geological constraints on the origin of oxygenic photosynthesis. *Photosynth. Res.* **107**, 11–36.
- Fischer W. W., Schroeder S., Lacassie J. P., Beukes N. J., Goldberg T., Strauss H., Horstmann U. E., Schrag D. P. and Knoll A. H. (2009) Isotopic constraints on the Late Archean carbon cycle from the Transvaal Supergroup along the western margin of the Kaapvaal Craton, South Africa. *Precambrian Res.* **169**, 15–27.
- Frei R., Gaucher C., Poulton S. W. and Canfield D. E. (2009) Fluctuations in Precambrian atmospheric oxygenation recorded by chromium isotopes. *Nature* **461**, 250–253.
- Garvin J., Buick R., Anbar A. D., Arnold G. L. and Kaufman A. J. (2009) Isotopic evidence for an aerobic nitrogen cycle in the latest Archean. *Science* **323**, 1045–1048.
- Godfrey L. V. and Falkowski P. G. (2009) The cycling and redox state of nitrogen in the Archean ocean. *Nat. Geosci.* **2**, 725–729.
- Goldberg T., Archer C., Vance D. and Poulton S. W. (2009) Mo isotope fractionation during adsorption to Fe (oxyhydr)oxides. *Geochim. Cosmochim. Acta* **73**, 6502–6516.
- Greber N. D., Hofmann B. A., Voegelin A. R., Villa I. M. and Nägler T. F. (2011) Mo isotope composition in Mo-rich high- and low-T hydrothermal systems from the Swiss Alps. *Geochim. Cosmochim. Acta* **75**, 6600–6609.
- Guilbaud R., Butler I. B. and Ellam R. M. (2011) Abiotic pyrite formation produces a large Fe isotope fractionation. *Science* **332**, 1548–1551.
- Hayes J. M. (1983) Geochemical evidence bearing on the origin of aerobicity, a speculative hypothesis. In *Earth's Earliest Biosphere, Its Origin and Evolution* (ed. J. W. Schopf). Princeton University Press, Princeton, NJ, pp. 291–301.
- Heimann A., Johnson C. M., Beard B. L., Valley J. W., Roden E. E., Spicuzza M. J. and Beukes N. J. (2010) Fe, C, and O isotope compositions of banded iron formation carbonates demonstrate a major role for dissimilatory iron reduction in ~2.5 Ga marine environments. *Earth Planet. Sci. Lett.* **294**, 8–18.
- Helz G. R., Miller C. V., Charnock J. M., Mosselmans J. F. W., Patrick R. A. D., Garner C. D. and Vaughan D. J. (1996) Mechanism of molybdenum removal from the sea and its concentration in black shales. *Geochim. Cosmochim. Acta* **60**, 3631–3642.
- Helz G. R., Bura-Nakić E., Mikac N. and Ciglenečki I. (2011) New model for molybdenum behavior in euxinic waters. *Chem. Geol.* **284**, 323–332.
- Hoashi M., Bevacqua D. C., Otake T., Watanabe Y., Hickman A. H., Utsunomiya S. and Ohmoto H. (2009) Primary hematite formation in an oxygenated sea 3.46 billion years ago. *Nat. Geosci.* **2**, 301–306.
- Holland H. D. (2006) The oxygenation of the atmosphere and oceans. *Philos. Trans. R. Soc. B* **361**, 903–915.
- Holland H. D. (1984) *The Chemical Evolution of the Atmosphere and Oceans*. Princeton University Press, Princeton, NJ.
- Johnson C. M., Beard B. L., Beukes N. J., Klein C. and O'Leary J. M. (2003) Ancient geochemical cycling in the Earth as inferred from Fe isotope studies of banded iron formations from the Transvaal Craton. *Contrib. Mineral. Petrol.* **144**, 523–547.
- Johnson C. M., Beard B. L., Klein C., Beukes N. J. and Roden E. E. (2008a) Iron isotopes constrain biologic and abiologic processes in banded iron formation genesis. *Geochim. Cosmochim. Acta* **72**, 151–169.
- Johnson C. M., Beard B. L. and Roden E. E. (2008b) The iron isotope fingerprints of redox and biogeochemical cycling in the modern and ancient Earth. *Annu. Rev. Earth Planet. Sci.* **36**, 457–493.
- Kappler A., Pasquero C., Konhauser K. O. and Newman D. K. (2005) Deposition of banded iron formations by anoxygenic phototrophic Fe(II)-oxidizing bacteria. *Geology* **33**, 865–868.
- Kashiwabara T., Takahashi Y. and Tanimizu M. (2009) A XAFS study on the mechanism of isotopic fractionation of molybdenum during its adsorption on ferromanganese oxides. *Geochem. J.* **43**, E31–E36.
- Kasting J. F. (1992) Models relating to Proterozoic atmospheric and ocean chemistry. In *The Proterozoic Biosphere, A Multidisciplinary Study* (eds. J. W. Schopf and C. Klein). Cambridge University Press, New York, pp. 1185–1187.
- Kaufman A. J., Johnston D. T., Farquhar J., Masterson A. L., Lyons T. W., Bates S., Anbar A. D., Arnold G. L., Garvin J. and Buick R. (2007) Late Archean biospheric oxygenation and atmospheric evolution. *Science* **317**, 1900–1903.
- Kendall B., Reinhard C. T., Lyons T. W., Kaufman A. J., Poulton S. W. and Anbar A. D. (2010) Pervasive oxygenation along late Archean ocean margins. *Nat. Geosci.* **3**, 647–652.

- Kim S. T. and O'Neil J. R. (1997) Equilibrium and nonequilibrium oxygen isotope effects in synthetic carbonates. *Geochim. Cosmochim. Acta* **61**, 3461–3475.
- Klein C. (2005) Some Precambrian banded iron-formations (BIFs) from around the world: their age, geologic setting, mineralogy, metamorphism, geochemistry, and origin. *Am. Mineral.* **90**, 1473–1499.
- Knoll A. H. and Beukes N. J. (2009) Introduction: Initial investigations of a Neoproterozoic shelf margin-basin transition (Transvaal Supergroup, South Africa). *Precambrian Res.* **169**, 1–14.
- Konhauser K. O., Hamade T., Raiswell R., Morris R. C., Ferris F. G., Southam G. and Canfield D. E. (2002) Could bacteria have formed the Precambrian banded iron formations? *Geology* **30**, 1079–1082.
- Kostka J. E. and Luther, III, G. W. (1994) Partitioning and speciation of solid phase iron in saltmarsh sediments. *Geochim. Cosmochim. Acta* **58**, 1701–1710.
- Kump L. R. and Barley M. E. (2007) Increased subaerial volcanism and the rise of atmospheric oxygen 2.5 billion years ago. *Nature* **448**, 1033–1036.
- Ledwell J. R., Watson A. J. and Law C. S. (1993) Evidence for slow mixing across the pycnocline from an open-ocean tracer-release experiment. *Nature* **364**, 701–703.
- Liermann L. J., Guynn R. L., Anbar A. and Brantley S. L. (2005) Production of a molybdophore during metal-targeted dissolution of silicates by soil bacteria. *Chem. Geol.* **220**, 285–302.
- McManus J., Nägler T. F., Siebert C., Wheat C. G. and Hammond D. E. (2002) Oceanic molybdenum isotope fractionation: diagenesis and hydrothermal ridge–flank alteration. *Geochem. Geophys. Geosyst.* **3**, 1078. <http://dx.doi.org/10.1029/2002GC000356>.
- Millero F. J., Sotolongo S. and Izaguirre M. (1987) The oxidation kinetics of Fe(II) in seawater. *Geochim. Cosmochim. Acta* **51**, 793–801.
- Morris R. C. and Horwitz R. C. (1983) The origin of the iron-formation-rich Hamersley Group of Western Australia – deposition on a platform. *Precambrian Res.* **21**, 273–297.
- Murray J. W. and Brewer P. G. (1977) Mechanism of removal of manganese, iron, and other trace metals from seawater. In *Marine Manganese Deposits* (ed. G. P. Glasby). Elsevier, Amsterdam, pp. 291–325.
- Nägler T. F., Neubert N., Böttcher M. E., Dellwig O. and Schnetger B. (2011) Molybdenum isotope fractionation in pelagic euxinia: evidence from the modern Black and Baltic Seas. *Chem. Geol.* **289**, 1–11.
- Neubert N., Nägler T. F. and Böttcher M. E. (2008a) Sulfidity controls molybdenum isotope fractionation into euxinic sediments: evidence from the modern Black Sea. *Geology* **36**, 775–778.
- Neubert N., Heri A. R., Nägler T. F., Böttcher M. E. and Villa I. M. (2008b) Refining sources and sinks in the global molybdenum cycle. *Geochim. Cosmochim. Acta* **72**, A676.
- Neubert N., Heri A. R., Voegelin A. R., Nägler T. F., Schlunegger F. and Villa I. M. (2011) The molybdenum isotopic composition in river water: constraints from small catchments. *Earth Planet. Sci. Lett.* **304**, 180–190.
- Ohmoto H. (1996) Evidence in pre-2.2 Ga paleosols for the early evolution of atmospheric oxygen and terrestrial biota. *Geology* **24**, 1135–1138.
- Ohmoto H., Watanabe Y., Yamaguchi K. E., Naraoka H., Haruna M., Kakegawa T., Hayashi K. and Kato Y. (2006) Chemical and biological evolution of early Earth: constraints from banded iron formations. In *Evolution of Early Earth's Atmosphere, Hydrosphere, and Biosphere – Constraints from Ore Deposits: Geological Society of America Memoir 198* (eds. S. E. Kesler and H. Ohmoto). Geological Society of America, Denver, pp. 291–331.
- Ono S., Beukes N. J. and Rumble D. (2009a) Origin of two distinct multiple-sulfur isotope compositions of pyrite in the 2.5 Ga Klein Naute Formation, Griqualand West Basin, South Africa. *Precambrian Res.* **169**, 48–57.
- Ono S., Kaufman A. J., Farquhar J., Sumner D. Y. and Beukes N. J. (2009b) Lithofacies control on multiple-sulfur isotope records and Neoproterozoic sulfur cycles. *Precambrian Res.* **169**, 58–67.
- Pavlov A. A. and Kasting J. F. (2002) Mass-independent fractionation of sulfur isotopes in Archean sediments: strong evidence for an anoxic Archean atmosphere. *Astrobiology* **2**, 27–41.
- Pearce C. R., Burton K. W., Pogge von Strandman P. A. E., James R. H. and Gíslason S. R. (2010) Molybdenum isotope behaviour accompanying weathering and riverine transport in a basaltic terrain. *Earth Planet. Sci. Lett.* **295**, 104–114.
- Pizarro J., Belzile N., Filella M., Leppard G. G., Negre J., Perret D. and Buffle J. (1995) Coagulation/sedimentation of submicron iron particles in a eutrophic lake. *Water Res.* **29**, 617–632.
- Planavsky N. J., Rouxel O. J., Bekker A., Lalonde S. V., Konhauser K. O., Reinhard C. T. and Lyons T. W. (2010a) The evolution of the marine phosphate reservoir. *Nature* **467**, 1088–1090.
- Planavsky N., Bekker A., Rouxel O. J., Kamber B., Hofmann A., Knudsen A. and Lyons T. W. (2010b) Rare Earth Element and yttrium compositions of Archean and Paleoproterozoic Fe formations revisited: new perspectives on the significance and mechanisms of deposition. *Geochim. Cosmochim. Acta* **74**, 6387–6405.
- Polyakov V. B. and Sultantov D. M. (2011) New data on equilibrium iron isotope fractionation among sulfides: constraints on mechanisms of sulfide formation in hydrothermal and igneous systems. *Geochim. Cosmochim. Acta* **75**, 1957–1974.
- Poulson R. L., Siebert C., McManus J. and Berelson W. M. (2006) Authigenic molybdenum isotope signatures in marine sediments. *Geology* **34**, 617–620.
- Poulton S. W. and Canfield D. E. (2005) Development of a sequential extraction procedure for iron; implications for iron partitioning in continentally derived particulates. *Chem. Geol.* **214**, 209–221.
- Rashby S. E., Sessions A. L., Summons R. E. and Newman D. K. (2007) Biosynthesis of 2-methylbacteriohopanepolyols by an anoxygenic phototroph. *Proc. Natl. Acad. Sci. USA* **104**, 15099–15104.
- Rasmussen B., Fletcher I. R., Brocks J. J. and Kilburn M. R. (2008) Reassessing the first appearance of eukaryotes and cyanobacteria. *Nature* **455**, 1101–1104.
- Reinhard C. T., Raiswell R., Scott C., Anbar A. D. and Lyons T. W. (2009) A late Archean sulfidic sea stimulated by early oxidative weathering of the continents. *Science* **326**, 713–716.
- Riley J. P. and Chester R. (1971) *Introduction to Marine Chemistry*. Academic Press, New York.
- Rouxel O. J., Bekker A. and Edwards K. J. (2005) Iron isotope constraints on the Archean and Paleoproterozoic ocean redox state. *Science* **307**, 1088–1091.
- Rye R. and Holland H. D. (1998) Paleosols and the evolution of atmospheric oxygen; a critical review. *Am. J. Sci.* **298**, 621–672.
- Schlesinger W. H. (1997) *Biogeochemistry – An Analysis of Global Change*. Academic Press, San Diego.
- Schröder S., Lacassie J. P. and Beukes N. J. (2006) Stratigraphic and geochemical framework of the Agouron drill cores, Transvaal Supergroup (Neoproterozoic–Paleoproterozoic, South Africa). *S. Afr. J. Geol.* **109**, 23–54.
- Severmann S., Johnson C. M., Beard B. L., German C. R., Edmonds H. N., Chiba H. and Green D. R. H. (2004) The effect

- of plume processes on the Fe isotope composition of hydrothermally derived Fe in the deep ocean as inferred from the Rainbow vent site, Mid-Atlantic Ridge, 36 degrees 14' N. *Earth Planet. Sci. Lett.* **225**, 63–76.
- Siebert C., Nägler T. F., von Blanckenburg F. and Kramers J. D. (2003) Molybdenum isotope records as potential new proxy for paleoceanography. *Earth Planet. Sci. Lett.* **211**, 159–171.
- Siebert C., McManus J., Bice A., Poulson R. and Berelson W. M. (2006) Molybdenum isotope signatures in continental margin marine sediments. *Earth Planet. Sci. Lett.* **241**, 723–733.
- Skulan J. L., Beard B. L. and Johnson C. M. (2002) Kinetic and equilibrium Fe isotope fractionation between aqueous Fe(III) and hematite. *Geochim. Cosmochim. Acta* **66**, 2995–3015.
- Stookey L. (1970) Ferrozine: a new spectrophotometric reagent for iron. *Anal. Chem.* **42**, 779–781.
- Sumner D. Y. and Beukes N. J. (2006) Sequence stratigraphic development of the Neoproterozoic Transvaal carbonate platform, Kaapvaal Craton, South Africa. *S. Afr. J. Geol.* **109**, 11–22.
- Taillefert M. and Gaillard J. F. (2002) Reactive transport modeling of trace elements in the water column of a stratified lake: iron cycling and metal scavenging. *J. Hydrol.* **256**, 16–34.
- Taylor S. R. and McLennan S. M. (1985) *The Continental Crust: Its Composition and Evolution*. Blackwell Scientific Publications, Oxford.
- Tossell J. A. (2005) Calculating the partitioning of the isotopes of Mo between oxidic and sulfidic species in aqueous solution. *Geochim. Cosmochim. Acta* **69**, 2981–2993.
- Towe K. M. (1994) Earth's early atmosphere: constraints and opportunities for early evolution. In *Early Life on Earth* (ed. S. Bengtson). Columbia University Press, New York, pp. 36–47.
- Trouwborst R. E., Johnston A., Koch G., Luther, III, G. W. and Pierson B. K. (2007) Biogeochemistry of Fe(II) oxidation in a photosynthetic microbial mat: implications for Precambrian Fe(II) oxidation. *Geochim. Cosmochim. Acta* **71**, 4629–4643.
- Veizer J., Clayton R. N., Hinton R. W., von Brunn V., Mason T. R., Buck S. G. and Hoefs J. (1990) Geochemistry of Precambrian carbonates: 3-shelf seas and non-marine environments of the Archean. *Geochim. Cosmochim. Acta* **54**, 2717–2729.
- Voegelin A. R., Nägler T. F., Beukes N. J. and Lacassie J. P. (2010) Molybdenum isotopes in late Archean carbonate rocks: implications for early Earth oxygenation. *Precambrian Res.* **182**, 70–82.
- Voegelin A. R., Nägler T. F., Samankassou E. and Villa I. M. (2009) Molybdenum isotopic composition of modern and Carboniferous carbonates. *Chem. Geol.* **265**, 488–498.
- Waldbauer J. R., Sherman L. S., Sumner D. Y. and Summons R. E. (2009) Late Archean molecular fossils from the Transvaal Supergroup record the antiquity of microbial diversity and aerobiosis. *Precambrian Res.* **169**, 28–47.
- Walker J. C. G. (1991) *Numerical Adventures with Geochemical Cycles*. Oxford University Press, Oxford.
- Wasylenki L. E., Anbar A. D., Liermann L. J., Mathur R., Gordon G. W. and Brantley S. L. (2007) Isotope fractionation during microbial metal uptake measured by MC-ICP-MS. *J. Anal. At. Spectrom.* **22**, 905–910.
- Watanabe Y., Farquhar J. and Ohmoto H. (2009) Anomalous fractionations of sulfur isotopes during thermochemical sulfate reduction. *Science* **324**, 370–373.
- Wiesli R. A., Beard B. L. and Johnson C. M. (2004) Experimental determination of Fe isotope fractionation between aqueous Fe(II), siderite and “green rust” in abiotic systems. *Chem. Geol.* **211**, 343–362.
- Wille M., Kramers J. D., Naegler T. F., Beukes N. J., Schröder S., Meisel T., Lacassie J. P. and Voegelin A. R. (2007) Evidence for a gradual rise of oxygen between 2.6 and 2.5 Ga from Mo isotopes and Re-PGE signatures in shales. *Geochim. Cosmochim. Acta* **71**, 2417–2435.
- Wu L., Beard B., Roden E. E. and Johnson C. (2011) Stable iron isotope fractionation between aqueous Fe(II) and hydrous ferric oxide. *Environ. Sci. Technol.* **45**, 1847–1852.
- Wu L., Beard B. L., Roden E. E., Kennedy C. B. and Johnson C. M. (2010) Stable Fe isotope fractionations produced by aqueous Fe(II)–hematite surface interactions. *Geochim. Cosmochim. Acta* **74**, 4249–4265.
- Yamaguchi K. E. (2002) *Geochemistry of Archean-Paleoproterozoic Black Shales: The Early Evolution of the Atmosphere, Oceans, and Biosphere*. Ph. D. thesis, Pennsylvania State University.
- Yamaguchi K., Johnson C., Beard B., Beukes N., Gutzmer J. and Ohmoto H. (2007) Isotopic evidence for iron mobilization during Paleoproterozoic lateritization of the Hekpoort paleosol profile from Gaborone, Botswana. *Earth Planet. Sci. Lett.* **256**, 577–587.
- Zerkle A. L., Scheiderich K., Maresca J. A., Liermann L. J. and Brantley S. L. (2011) Molybdenum isotope fractionation by cyanobacterial assimilation during nitrate utilization and N₂ fixation. *Geobiology* **9**, 94–106.

Associate editor: Derek Vance